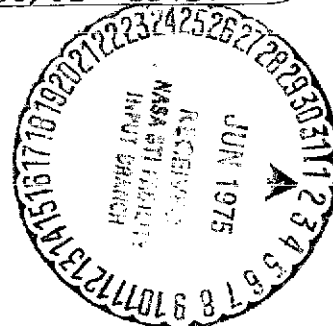(NASA-CR-137646) · CALCULATION OF STATIC
LONGITUDINAL AERODYNAMIC CHARACTERISTICS OF
STOL AIRCRAFT WITH UPPER-SURFACE BLOWN FLAPS
(Nielsen Engineering and Research, Inc.)
63 p HC $4.25   CSCL 20D

N75-23483

Unclas
G3/02 22427

NIELSEN ENGINEERING
AND RESEARCH, INC.

CES: 510 CLYDE AVENUE / MOUNTAIN VIEW, CALIFORNIA 94043 / TELEPHONE (415) 968-9457

NASA CR-137646

CALCULATION OF STATIC LONGITUDINAL

AERODYNAMIC CHARACTERISTICS

OF STOL AIRCRAFT WITH

UPPER-SURFACE-BLOWN FLAPS

by M. R. Mendenhall, S. C. Perkins, Jr.,
F. K. Goodwin, and S. B. Spangler

NEAR TR 83

April 1975

TABLE OF CONTENTS

CALCULATION OF STATIC LONGITUDINAL AERODYNAMIC CHARACTERISTICS OF STOL AIRCRAFT WITH UPPER-SURFACE-BLOWN FLAPS

by M. R. Mendenhall, S. C. Perkins, Jr.,
F. K. Goodwin, and S. B. Spangler
Nielsen Engineering & Research, Inc.

SUMMARY

An existing prediction method developed for EBF aircraft configurations was applied to USB configurations to determine its potential utility in predicting USB aerodynamic characteristics. An existing wing-flap vortex-lattice computer program was modified to handle multiple spanwise flap segments at different flap angles, an arrangement typical of USB configurations currently under investigation. A potential flow turbofan wake model developed for circular cross-section jets was used to model a rectangular cross-section jet wake by placing a number of circular jets side by side. The calculation procedure was evaluated by comparison of measured and predicted aerodynamic characteristics on a variety of USB configurations. The method is limited to the case where the flow and geometry of the configuration are symmetric about a vertical plane containing the wing root chord.

Comparison of predicted and measured lift and pitching moment coefficients were made on swept wings with one and two engines per wing panel, various flap deflection angles, and a range of thrust coefficients. The results indicate satisfactory prediction of lift for flap deflections up to 55° and thrust coefficients less than 2. At higher flap angles and higher thrusts, the method begins to overpredict lift, probably due to flow separation from the wing and flaps. Pitching-moment coefficients are generally not predicted well for power-on conditions, an indication that the distribution of loading on the wing and flap is not correctly predicted.

The applicability of the prediction procedure to USB configurations is evaluated, and specific recommendations for improvements are discussed.

INTRODUCTION

The increased interest in STOL jet transport aircraft has led to the development of externally blown jet flaps as a means of achieving the high lift coefficients required for STOL operation. The usual scheme is to use

the available engine thrust for lift augmentation and propulsion concurrently. Two external flow concepts being given serious consideration are shown in figure 1. The first is the externally blown flap (EBF) configuration in which the entire jet efflux from pod-mounted turbofan engines beneath the wing is made to impinge on a large, highly deflected, multiply slotted flap system. The second concept is the upper-surface-blown(USB) flap in which the entire jet efflux from engines mounted over the wing is directed at the wing upper surface. The jet exhaust becomes attached to the wing upper surface and follows the deflected trailing-edge flap through the Coanda effect. This latter concept is attractive in that the wing acts as a shield for downward propagating noise.

At the present time, few analytical methods are available for predicting the aerodynamic performance of USB configurations and these are generally restricted to thin jets. A method was developed for EBF configurations in which the lift and pitching moment on the wing-flap with engine-wake interference is calculated using potential flow lifting-surface and engine-wake models (ref. 1). The same general approach to the calculation of USB wake-wing interference was considered promising. Consequently, an exploratory study was undertaken to determine the applicability of the methods of reference 1 to USB configurations. This report presents the results of that study.

The wing-flap vortex-lattice program of reference 1 was modified to handle configurations with multiple spanwise flap segments at different flap angles and breaks in leading-edge and trailing-edge sweep angle. These changes were dictated by the type of configuration for which data are available. The engine-wake model of reference 1, which is applicable to circular cross-section jets, was used in its original form by placing several circular jets side by side to approximate the typically rectangular USB wake jets. The major part of the study was directed towards investigating jet placement and spreading effects, as evaluated by comparisons between predicted and measured forces and moments. The methods and results are presented, together with comments concerning improvements necessary to develop the method into a usable engineering prediction method.

2

SYMBOLS

A_f	fan exit flow area
A_j	jet-wake cross-sectional area at beginning of the wake
b	wing span
C_J	thrust coefficient, T/qS
C_L	lift coefficient, L/qS
C_m	pitching-moment coefficient, $M/qS\bar{c}$
c	chord of area element on the wing
$\bar{c}$	mean aerodynamic chord
c_ℓ	section-lift coefficient, based on local chord
E	jet expansion rate, R_Γ/R_o, figure 4
F_u, F_v, F_w	backwash, sidewash, and downwash influence coefficient for a horseshoe vortex
L	lift force
M	pitching moment; or number of vortices or control points on wing
m	jet velocity ratio, V/V_j
N	number of circular jets representing rectangular jet
NF	number of vortices or control points on flap
NFLAPS	number of flaps
q	free-stream dynamic pressure, $\frac{1}{2}\rho_\infty V^2$
R	radius of jet wake
R_Γ	local radius of vortex ring
R_o	radius of jet wake at beginning of jet wake
S	wing planform area used as reference area by wing-flap program

T	engine thrust
u,v,w	perturbation velocities in x, y and z directions, respectively
u_i,v_i,w_i	perturbation velocities in x, y and z directions, respectively, induced on wing-flap by other airframe components
V	free-stream velocity
V_f	fan exit velocity
V_j	jet velocity directed along the geometric engine centerline at beginning of wake (includes free-stream velocity)
X,Y,Z	coordinates with origin located at the wing root chord nose, figure 2; X axis coincident with wing root chord, positive forward; Y axis positive right; and Z axis positive in downward direction
x,y,z	local coordinate system located at the midspan of a horseshoe vortex on the wing and with the same directions as X,Y,Z coordinate system; or jet-wake coordinate system fixed at beginning of jet
$Y_{\mathbb{C}_L}$	lateral coordinate measured from center of rectangular jet
α	angle of attack of wing root chord with respect to free stream, degrees
α_ℓ	angle between tangent to mean camber surface of the wing and X direction, degrees
β	angle used in jet centerline specification, figure 6
Γ	vortex strength of a horseshoe vortex
Γ_j	vortex strength of vortex rings used to model expanding jet wake
γ	vortex strength of vortex cylinder used to model straight jet wake
Δs	vortex ring spacing, figure 3
δ_f	flap deflection angle measured perpendicular to the hingeline, positive downward, degrees
δ_ℓ	angle between tangent to mean camber surface and the root chord plane, degrees
δ_{xz}	streamwise flap deflection angle measured in a plane parallel to the X-Z plane, positive downwards, degrees

4

η	nondimensional spanwise coordinate, $Y/(b/2)$
θ	angle of inclination of jet-wake centerline, relative to X direction, degrees
ν	control point index in equations (1) and (2)
ρ_f	jet density at fan exit
ρ_∞	free-stream density
ϕ	dihedral of wing, degrees

Subscripts

$\mathcal{L}$	centerline
f	flap
ℓ	left; or local
o	initial
W	wing

THEORETICAL APPROACH

Wing-Flap Model

In reference 1, a three-dimensional horseshoe vortex lattice is used as the distribution of singularities representing the wing and flap lifting surfaces. This prediction method includes in its boundary condition the mutual interference between the wing and flap surfaces and any external source of perturbation velocities. The flow tangency condition is applied at a finite number of control points on the wing and flap surfaces, which results in a set of simultaneous equations from which the vortex strengths are determined. The computer program described in reference 1 has the limitation of considering only one trailing-edge flap with uniform spanwise deflection. Multiple chordwise flap segments are handled through a camber distribution on a mean flap surface. Typical USB configurations have two or three spanwise flap segments at different deflection angles and each spanwise segment is usually made up of multiple flap elements of different sizes. It was decided that better comparisons with experiment could be achieved if the flap geometry limitation in the original program were removed. The program was modified and the configuration parameters included in the method are listed below.

5

Wing Panels

Mean camber surface: May have both camber and twist

Leading-edge shape: May have up to 20 breaks in sweep

Trailing-edge shape: Same as for leading edge

Taper: Variable

Tips: Parallel to root chord

Dihedral: Constant over semispan

Thickness: Neglected

Flaps

Number: Up to 10 individual flap elements

Location: At or near wing trailing edge; gaps between flaps are
permitted

Mean camber surface: Each individual flap may have camber

Span: Full or partial span

Leading-edge shape: Straight line which may be swept

Trailing-edge shape: Same as for leading edge

Taper: Linear

Deflection: Each flap may have a different deflection angle

Thickness: Neglected

The method is restricted to flow in the pitch plane; yaw effects are
not included. Since large flap deflection angles are used only at low
speeds, compressibility effects are not included. Configuration angle of
attack and flap deflection angles are accounted for in the boundary condi-
tions in terms of trigonometric functions instead of linear terms since the
magnitude of these angles can be large. Finally, since potential flow
theory is used throughout, the methods cannot account for separation or
other viscous effects.

Boundary condition.- The wing and flap panels are divided into
trapezoidal area elements. A horseshoe vortex is placed in each area
element such that the spanwise bound leg lies along the element quarter
chord and its trailing legs lie along the chordwise sides of the element

6

with the trailing legs extending to infinity in the plane of the area
element (fig. 2). This is the same lifting-surface model used in refer-
ence 1. The area elements on each individual lifting surface, wing or
flaps, have uniform chordwise length at any spanwise station, but the span-
wise widths may vary to allow closer spacing in regions where large loading
gradients exist.

The flow tangency boundary condition is applied at the midpoint of
the three-quarter chord of each area element. The boundary condition for
the νth control point on the left wing panel is formulated as follows.

$$\sum_{n=1}^{M} \frac{\Gamma_n}{4\pi V} \left(F_{w_{\nu,n}} \cos \phi_\nu \cos \alpha_{\ell_\nu} - F_{v_{\nu,n}} \sin \phi_\nu \cos \alpha_{\ell_\nu} + F_{u_{\nu,n}} \sin \alpha_{\ell_\nu} \right)$$

$$+ \sum_{j=1}^{NFLAPS} \sum_{n=1}^{NF(j)} \frac{\Gamma_n}{4\pi V} \left[F_{w_f,\nu,n} \left(\cos \phi_\nu \cos \alpha_{\ell_\nu} \cos \delta_{xz_j} + \sin \alpha_{\ell_\nu} \sin \delta_{xz_j} \right) \right.$$

$$\left. - F_{v_f,\nu,n} \sin \phi_\nu \cos \alpha_{\ell_\nu} + F_{u_f,\nu,n} \left(\sin \alpha_{\ell_\nu} \cos \delta_{xz_j} - \cos \phi_\nu \cos \alpha_{\ell_\nu} \sin \delta_{xz_j} \right) \right]$$

$$= \left(\sin \alpha - \frac{w_{i,\nu}}{V} \right) \cos \phi_\nu \cos \alpha_{\ell_\nu} + \frac{v_{i,\nu}}{V} \sin \phi_\nu \cos \alpha_{\ell_\nu} + \left(\cos \alpha - \frac{u_{i,\nu}}{V} \right) \sin \alpha_{\ell_\nu}$$

$$\nu = 1,2,\ldots M \tag{1}$$

where $\quad$ M = number of horseshoe vortices on the wing

$\quad$ NFLAPS = number of flaps

$\quad$ NF(j) = number of horseshoe vortices on j^{th} flap

Similarly, the boundary condition for the νth control point on the
i^{th} flap can be written as

$$\sum_{n=1}^{M} \frac{\Gamma_n}{4\pi V} \left[F_{w_{\nu},n} \left(\cos \phi_{f_{\nu}} \cos \delta_{\ell_{\nu}} \cos \delta_{xz_i} - \sin \delta_{\ell_{\nu}} \sin \delta_{xz_i} \right) \right.$$

$$\left. - F_{v_{\nu},n} \sin \phi_{f_{\nu}} \cos \delta_{\ell_{\nu}} + F_{u_{\nu},n} \left(\sin \delta_{\ell_{\nu}} \cos \delta_{xz_i} + \cos \phi_{f_{\nu}} \cos \delta_{\ell_{\nu}} \sin \delta_{xz_i} \right) \right]$$

$$+ \sum_{j=1}^{NFLAPS} \sum_{n=1}^{NF(j)} \frac{\Gamma_n}{4\pi V} \left\{ F_{w_{f_j},\nu,n} \left[\cos \phi_{f_{\nu}} \cos \delta_{\ell_{\nu}} \cos \left(\delta_{xz_i} - \delta_{xz_j} \right) \right. \right.$$

$$\left. - \sin \delta_{\ell_{\nu}} \sin \left(\delta_{xz_i} - \delta_{xz_j} \right) \right] - F_{v_{f_j},\nu,n} \sin \phi_{f_{\nu}} \cos \delta_{\ell_{\nu}}$$

$$\left. + F_{u_{f_j},\nu,n} \left[\sin \delta_{\ell_{\nu}} \cos \left(\delta_{xz_i} - \delta_{xz_j} \right) + \cos \phi_{f_{\nu}} \cos \delta_{\ell_{\nu}} \sin \left(\delta_{xz_i} - \delta_{xz_j} \right) \right] \right\}$$

$$= \sin \left(\alpha + \delta_{xz_i} \right) \cos \phi_{f_{\nu}} \cos \delta_{\ell_{\nu}} + \cos \left(\alpha + \delta_{xz_i} \right) \sin \delta_{\ell_{\nu}}$$

$$- \frac{w_{i,\nu}}{V} \left(\cos \phi_{f_{\nu}} \cos \delta_{\ell_{\nu}} \cos \delta_{xz_i} - \sin \delta_{\ell_{\nu}} \sin \delta_{xz_i} \right) + \frac{v_{i,\nu}}{V} \sin \phi_{f_{\nu}} \cos \delta_{\ell_{\nu}}$$

$$- \frac{u_{i,\nu}}{V} \left(\sin \delta_{\ell_{\nu}} \cos \delta_{xz_i} + \cos \phi_{f_{\nu}} \cos \delta_{\ell_{\nu}} \sin \delta_{xz_i} \right) \tag{2}$$

The right-hand sides of equations (1) and (2) represent the free-stream component and the externally induced perturbation velocities normal to the wing and flap chordal planes. The functions F_u, F_v, F_w are influence functions relating the velocity components induced at some point by a horseshoe vortex to the circulation strength and position of the point relative to the origin of the vortex coordinate system. These relationships are obtained from the Biot-Savart law. The influence functions used in the present vortex-lattice method are the same as those given in equations (4), (5), and (6) of reference 1.

Loading distribution.- Once the circulation values have been calculated, the load distribution on the lifting surfaces can be obtained by means of the Kutta-Joukowski law for the aerodynamic force on a vortex

filament. The force on a vortex filament is the product of the density, velocity, and circulation strength; and its direction is normal to the velocity vector and the direction of the vorticity. As is described in reference 1, the lift and streamwise force components are calculated as the sum of two contributions: lift and streamwise force acting on the bound leg plus lift force acting on that portion of the trailing legs within the area element. The expressions for these forces are given by equations (9) and (10) of reference 1. In the formulation of the loads on the flap in reference 1, the sidewash velocities were omitted for reasons described. In the present formulation, these sidewash velocities have been retained in the loads calculation for the sake of completeness. Whether or not these sidewash velocities are included has very little effect on the total force coefficients, but it does have some effect on the distribution of forces.

Jet-Wake Model

In reference 1, a potential flow model of the wake of a turbofan engine is described. The wake boundary is represented by an expanding circular cylinder stretching between the jet engine exhaust and some point a large distance downstream of the wing and flap. A continuous vorticity distribution is placed on the specified jet boundary. The strength of the vorticity is determined by the momentum in the jet, which is assumed constant everywhere inside the jet. The computation is carried out by replacing the continuous vorticity distribution with a series of vortex rings coaxial with the jet centerline. Each ring represents a finite increment of length along the jet and the ring strength is equal to the net vorticity on the incremental length of the boundary. This model is shown schematically in figure 3. Also shown in this figure are typical velocity profiles at three stations along an expanding circular jet. The vortex ring model predicts nearly uniform velocity across the jet radius and the average velocity inside the jet boundary decreases with axial distance along the jet centerline in almost inverse proportion with the jet radius. The equations for the velocity field induced by a vortex ring or series of vortex rings are given in reference 1.

The potential flow model of the jet wake requires that the wake boundary be specified a priori. The description of an axisymmetric coflowing jet presented in reference 2 is used to define the particular

flow model. Theoretical spreading rates for various jet velocity ratios are shown in figure 4.

A typical USB configuration utilizes a rectangular shaped exhaust nozzle to direct the jet efflux over the top of the wing. One of the purposes of the present investigation is to use the axisymmetric jet potential flow model to approximate the effect of a rectangular shaped jet. To do this correctly, the mass, momentum, and region of influence of the rectangular jet should be modeled as closely as possible.

A rectangular shaped cross section can be approximated with one or more circles as shown in the sketch below. The velocity at the jet exit
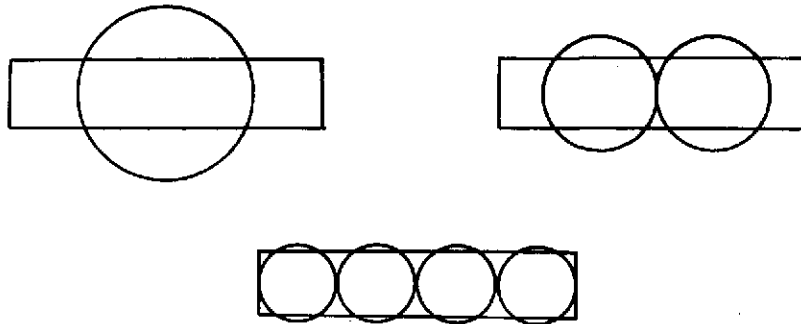
is matched if the area of the circle(s) is the same as the area of the rectangle, and the total momentum in the circular jets is the same as the momentum in the rectangular jet. If the far velocity field were of interest, the single circular jet would be a reasonable approximation to the rectangular jet. However, in the USB case, the jet is immediately adjacent to the wing and flap surfaces and the jet-induced flow field near the jet boundary determines the interference on the lifting surfaces. Thus, the lower figure in the preceding sketch is the better approximation to a high-aspect-ratio rectangular jet.

The approach taken in this investigation is to model the rectangular jet with an appropriate number of circular jets such that the width and height of the original jet are matched as nearly as possible. The total cross-sectional area of the circular jets matches the rectangular area, and the total momentum in the circular jets is the same as the momentum in the rectangular jet.

10

The strength of the vorticity representing the circular jets is calculated by the procedure described in reference 1 if a cold jet is assumed. The strength of a vortex ring at any point along the jet is

$$\frac{\Gamma_j}{V} = \frac{\gamma}{V} \frac{R_o}{R_\Gamma} \Delta s \tag{3}$$

where γ/V is the strength of the vortex cylinder, with radius, R_o, corresponding to the specified thrust coefficient. This vortex strength is

$$\frac{\gamma}{V} = \frac{V_j}{V} - 1 \tag{4}$$

where V_j is an average velocity across a jet area A_j. A_j and V_j correspond to the point where the jet becomes free, bounded only by the wing and flap surfaces. Assuming an incompressible jet, the velocity ratio, V_f/V, at the fan exit, A_f, is obtained from momentum considerations and is given by the approximate relationship

$$\frac{V_f}{V} = \frac{1}{2} \left[1 + \sqrt{1 + 2\left(\frac{SC_J}{A_f}\right)} \right] \tag{5}$$

When this velocity is expanded from the fan exit area to the wake area, the needed jet velocity ratio is

$$\frac{V_j}{V} = \frac{V_f}{V}\left(\frac{A_f}{A_j}\right) \tag{6}$$

The initial radius of each of the N circular jets describing the rectangular jet with initial area A_j is

$$R_o = \sqrt{\frac{A_j}{N\pi}} \tag{7}$$

If a hot, compressible jet is being considered, equation (5) may introduce errors into the jet velocity calculation. Assuming that $V_f/V \gg 1$, the velocity at the fan exit is approximately

$$\frac{V_f}{V} = \sqrt{\frac{C_J}{2} \frac{\rho}{\rho_f} \frac{S}{A_f}} \tag{8}$$

11

Equations (4), (6), and (7) supply the needed quantities to specify the jet strength.

Specification of the spreading rate of the jet model is an important part of the prediction method, as the spreading rate determines the rate of entrainment of mass into the jet which in turn determines the induced velocity field in the vicinity of the jet. The spreading rate also has a direct effect on the magnitude of the axial velocity at any point inside the jet. In the EBF method of reference 1, the jets were circular in cross section and the curves in figure 4 could be used to specify spreading rates. In the case of coflowing rectangular jets, no experimental or analytical spreading rate data are available. Some data on a rectangular jet exhausting into still air are available in references 3 and 4. These data indicate that the cross-sectional area of the rectangular jet expands more rapidly with distance downstream than does the area of an equivalent circular jet with the same initial area. At the present time, there is no rational method of correcting the coflowing circular jet spreading rates in figure 4 so that they are applicable to coflowing rectangular jets. For the current investigation, the spreading rates of figure 4 were used for each of the circular jets modeling the rectangular jet and the effect of increased spreading rates was examined in a parametric fashion.

Another important parameter is the location of the circular jets with respect to the wing and flap surfaces. In the EBF examples of reference 1, the centerline of the single circular jet was allowed to follow local streamlines. Performing a series of iterations on the position of the jet centerline showed that convergence could be obtained in four to five iterations and the final position of the centerline was approximately where it was placed before iteration (ref. 5). The same procedure could be followed for the USB calculations, but in the interest of doing the calculation as efficiently as possible, the following method was used. Assuming that the jet is turned around the flap by the Coanda effect and is attached to the wing and flap surfaces, the jet boundaries are positioned tangent to the wing and flaps as shown in figure 5. Since the spreading rates are known, the jet tangency condition specifies the vertical position of the centerline. Aft of the last flap, the centerline is allowed to return to the free-stream direction in a smooth fashion.

The uniform character of the jet model velocity profiles shown in figure 3 requires careful positioning of the centerline with respect to

12

the wing and flap surfaces. If the jet boundary is tangent to the lifting surfaces, the jet-induced axial velocity is approximately half the axial velocity in the uniform velocity region of the jet. A small movement of the jet away from the lifting surfaces results in a large reduction in the axial velocity; conversely, a small change in position of the jet toward the lifting surfaces can cause the axial velocities to increase.

It is an interesting characteristic of the prediction method that the circulation on the lifting surface is not sensitive to small changes in the vertical position of the jet, but the normal force is very sensitive to jet position. The circulation is proportional to the jet-induced upwash on the wing and the normal force is proportional to the product of the circulation and the jet-induced axial velocity. Jet-induced upwash near the jet boundary is not sensitive to small changes in vertical position; but as shown in figure 4, jet-induced axial velocity near the jet boundary is quite sensitive to small changes in vertical position. For this reason, the jet centerline was positioned with the jet boundary tangent to the lifting surfaces, and the effect of various jet vertical positions was examined parametrically.

A large amount of lateral spreading of the jet has been observed on USB configurations. The jet exhaust spreads in both an inboard and outboard direction although the greatest amount of spanwise flow appears to move outboard. The normal axisymmetric jet spreading of each of the circular jets modeling the rectangular jet accounts for some spanwise spreading of the jet, even if the individual circular jet centerlines move aft at a constant semispan position. The capability is included in the method to allow the jet centerline to move in a spanwise direction to cover any portion of the wing and flap surfaces.

Interference Flow Model

Calculation of the aerodynamic loading on a wing-flap configuration under the influence of the jet wake of a turbofan engine requires the combination of the two potential flow models just described. The lattice arrangement on the wing and flap lifting surfaces is chosen using the guidelines prescribed in reference 1. The lattice is nearly uniform in all regions of the wing and flaps not directly influenced by the jet wake, and in those regions in which the jet impinges directly on the wing and

flaps, the lattice spacing is reduced to one-half or one-quarter the normal spacing on the wing and flaps. One change in the lattice spacing required for USB models that is not needed for the EBF method in reference 1 is the following. Since the rectangular nozzle is modeled by a series of adjacent circular jets, the lattice spacing should be such that each circular jet centerline is directly above a row of control points. The problems arising from a different arrangement of jet centerlines and lattice spacing are described in a following section of this report. A typical lattice layout is discussed in the Results section.

The wing-flap loading is not considered to affect the engine thrust, the velocity distribution in the wake, nor the position of the jet center-line. This latter assumption is an additional restraint which was not imposed in the calculations of reference 1. This restriction on the jet centerline is made because the USB jet position with respect to the wing is assumed to be known; that is, the jet is attached and tangent to the wing and flaps between the engine exit and the trailing edge of the last flap. This was not the case in the former EBF calculations where the jet was not bounded by a solid surface and its position had to be found by iteration.

A schematic of the jet and wake model and its position with respect to the wing and flaps of a USB configuration is shown in figure 5. Two jet wakes are illustrated in which there is no lateral motion of the centerlines but each jet expands according to a prescribed spreading rate (fig. 4). The jets start at a point ahead of the wing corresponding to the inlet location of the engine and continue to the engine exit position, keeping a constant radius. The jet is positioned in this manner to reduce the effect of the large inflow induced near the beginning of the vortex ring wake model. The induced flow field near the beginning of the jet has the appearance of an engine inlet; therefore, the model is placed accord-ingly. At the engine exit position, the jet boundary is allowed to expand in some prescribed manner as shown in figure 5. The jet is allowed to extend downstream aft of the last flap a distance approximately equal to one wing chord.

In order to insure that the circular jet is tangent to the wing and flaps, the following method is used to locate points on the centerline. This method requires knowledge of the position of the leading edges of the

14

wing and flaps, the position of the trailing edge of the last flap, the flap angles, and the expansion rate of the jet as a function of distance along the jet. A typical wing-flap combination at a particular station is shown in figure 6. Given the proper expansion rate, E, and the initial radius of the jet, R_o, the local jet radius, R_Γ, can be found from the relationship

$$R_\Gamma = ER_o \qquad (9)$$

As shown in figure 6, two lines of length R_Γ are drawn at the point X_f, Z_f, one normal to each flap surface. Normals are drawn from the ends of each of these lines, and the point of their intersection is the desired position $(X_{\mathbb{C}}, Z_{\mathbb{C}})$ of the centerline for the given flap leading-edge position (X_f, Z_f).

Analytically, the method is as follows. Given δ_1 and δ_2, the deflection angles of flap 1 and flap 2, respectively, the angle β_1 is given by

$$\beta_1 = \frac{\delta_2 - \delta_1}{2} \qquad (10)$$

A new radius, R, shown in figure 6 is thus

$$R = \frac{R_\Gamma}{\cos \beta_1} \qquad (11)$$

and the angle between R and the normal to the wing chord plane is

$$\beta_2 = \delta_1 + \beta_1 \qquad (12)$$

The position of the point on the centerline, $(X_{\mathbb{C}}, Z_{\mathbb{C}})$, can be found as follows.

$$X_{\mathbb{C}} = X_f - R_\Gamma \frac{\sin \beta_2}{\cos \beta_1} \qquad (13)$$

$$Z_{\mathbb{C}} = Z_f - R_\Gamma \frac{\cos \beta_2}{\cos \beta_1} \qquad (14)$$

15

This procedure is followed at each point on the wing and flaps where a discontinuity in deflection angle occurs. At the trailing edge of the last flap, the centerline point is positioned by the magnitude of the jet radius, R_Γ, as shown in figure 6. The centerline position is completed by extrapolating it downstream and allowing it to approach the free-stream direction within a distance of one root chord length.

RESULTS

The results of applying the EBF prediction method of reference 1 to USB configurations are presented in the following way. First, the power-off wing-flap characteristics and the approximation of the rectangular jet by circular jets are described. On the basis of these results, certain basic decisions are made, and the method is applied to the twin-engine USB transport model of reference 6. Parametric changes in certain aspects of the model are made to investigate the sensitivity of the results to these changes. The most promising approach to the model is then selected and applied to two-engine and four-engine configurations for comparison with measured results.

Wing-Flap and Jet Models

Wing-flap characteristics.- The vortex-lattice program was used to predict the power-off characteristics of the two-engine model of reference 6. This model has an aspect ratio 7.28, tapered wing with a quarter chord sweep of 25°. Full-span leading-edge slats, deflected approximately 50°, were attached to the wing for all tests. The trailing-edge flap arrangement consisted of a Coanda plate extending from $\eta = 0.11$ to $\eta \approx 0.48$, a double-slotted flap from $\eta \approx 0.48$ to $\eta = 0.75$, and a slotted aileron from $\eta = 0.75$ to $\eta = 1.0$. The aileron was deflected 20° in all tests, and the Coanda plate was tested at deflection angles of 30°, 55°, and 75°. The slotted flaps have corresponding deflection angles of 12°, 27.5°, and 44°. The propulsion system consisted of one JT15D-1 engine in a nacelle attached to each wing panel at $\eta = 0.256$. The jet exhausted through a 0.72-foot by 2.64-foot rectangular nozzle with a deflector to direct the flow at the wing upper surface. The fuselage had a constant 4.0-foot diameter with tapered nose and tail. All data considered in this report were taken with the horizontal tail removed. Boundary-layer control was not used in any of the tests reported in reference 6.

16

The lattice arrangement chosen for this wing and flap configuration is shown in figure 7. As recommended in reference 1, the lattice has a fine mesh in the vicinity of the jet wake and a coarser mesh in the regions of lesser jet influence. The flaps are shown in an undeflected position to illustrate their true size and the relative sizes of the individual lattice elements. For accuracy in modeling the large Coanda plate, it was divided into three separate segments with no gaps separating the segments. The wing was considered to pass through the fuselage and no estimates were made for body lift and moment other than this approximate way of handling body lift carryover.

Comparison of measured lift and pitching moment of the wing-body with predicted values for the wing alone are shown in figure 8. Generally, the predicted lift values show the correct magnitude at the two lower flap angles. At the highest flap angle, the predicted values are high. The fact that the measured lift for 75⁰ is essentially the same as that for 55⁰ indicates that there was separation on the flaps at the higher angle. The predicted lift curves show a linear range at low angles of attack and nonlinear effects at the higher angles due to use of trigonometric angle functions. The data do not show any linear range. The predicted lift curve slopes agree well at moderate angles of attack up to wing stall.

The predicted pitching moments show the correct slope with lift coefficient, but the values are more negative than are the measured values. It is probable that the normal force on the fuselage and nacelles contribute a nose-up moment which would account for much of the discrepancy, but this was not estimated due to the complexity of the shapes. There is also a ram drag effect at the nacelle inlets which will contribute a nose-up pitching moment.

Jet characteristics.- The USB model described in reference 6 has one turbojet engine attached to each wing with the jet exhausting through a rectangular shaped nozzle lying directly on the upper wing surface. The engine exit is modeled by four equal area circular jet wakes as shown in figure 9(a). The total area and momentum of the circular jets is the same as the area and momentum of the rectangular jet. The circular jets are tangent to each other at the jet exit and assuming the centerlines to move aft at constant semispan stations, the jets begin to overlap as shown in figure 9(b). This overlapping can cause unusual velocity profiles inside

the jets, but this has little effect on the predicted aerodynamic coeffi-
cients of USB configurations. More important to these calculations is the
jet-induced flow field on the upper surfaces of the wing and flaps, which
is dependent on the jet overlapping and the size of the small void areas
between the wing upper surface and the boundary of the circular jets. These
void regions are pointed out in figure 9(b).

The cross section of the jet model with undisplaced centerlines is
shown again at the top of figure 9(c); because of symmetry, only the out-
board half of the jet is shown. The lower curve in figure 9(c) is the
induced axial velocity at the centerline of the jet model. The superposi-
tion of the individual circular jets modeling the rectangular jet causes
the unusual steps in the axial velocity profile inside the overlap areas.
Shown for comparison purposes on this figure is the average velocity
profile obtained from integration of rake data from reference 5. These
rake data were obtained under static conditions with the jet operating at
1700 pounds thrust. For purposes of comparison in this figure, the measured
average velocity profile is normalized by an assumed free-stream velocity
of 63 feet per second which corresponds to $q \approx 4.8$ psf and $C_J \approx 3.5$. The
magnitude of the predicted velocity profile, excluding the overlap region,
is in good agreement with the experimentally obtained profile. This is a
good indication that the jet model has the correct momentum and that the
assumed expansion rate and associated mass entrainment are in reasonable
agreement with those of the actual jet.

As mentioned earlier, the induced velocity field on the wing surface
determines the circulation and force distributions on the lifting surface.
Directly below the sketch of the jet cross section in figure 9(c) is the
induced upwash on the wing surface as predicted by the vortex ring model.
This curve is smooth with only a small indication of the effect of the
void regions in the jet; thus, the predicted circulation distribution on
the wing should show a smooth variation on the portion of the wing beneath
the jet.

The induced axial velocity from the vortex ring model will not have
a smooth distribution on the wing surface. The uniform character of the
axial velocity profile inside the circular jet (fig. 3) produces nearly
zero induced axial velocity in the void regions of the jet model. Large
axial velocities on the wing surface typical of those expected for USB

18

configurations occur only on the very limited portion of the wing directly beneath the centerline of each circular jet; that is, where the vortex rings are tangent to the lifting surface. For consistency, then, the control points of the vortex-lattice method should lie on the lines of tangency between the jets and the wing. No control points should fall inside the void area between the tangency lines. The number and location of the circular jets modeling the rectangular jet dictates the lattice arrangement on the wing in the vicinity of the jet as shown in figure 7.

The axial velocity induced on the wing by the jet acts on the wing bound vortex legs to produce a high loading. Thus, the jet-induced loads are sensitive to the height of the jet boundary above the wing because of the steep axial velocity gradient at the jet boundary.

The above restriction on the relative position of the jet centerlines and the lattice control points limit the prediction procedure in another area of interest. It is known that the jets of USB configurations spread laterally to cover a large portion of the wing and flap aft of the engine exit. The requirement that the jet centerlines and the lattice control points lie at the same semispan location prevents the jets from being moved in a spanwise direction. Thus, the bulk of the jet interference on the wing is forced to occur on the region of the wing and flap directly aft of the engine exit. A solution for this problem lies in the use of a rectangular shaped vortex singularity for the jet model. The rectangular jet model, with one side tangent to the upper surfaces of the wing and flaps, would have no void regions between the wing and the jet boundary; thus, the jet could move laterally as exhibited by experimental observations.

Parametric Investigation

In applying the existing prediction procedure to USB configurations, a number of geometric properties of the flow models must be given some consideration. These include the effect of the nacelles on the wing loading, the height of the jet boundary relative to the lifting surface, the placement of the jet centerline with respect to the lifting surface, and the spreading rate of the individual circular jets. Each of these items is examined on one particular configuration at a specified thrust coefficient. In this manner, the choice of the above parameters is made

with cognizance of their individual effect on the final predicted charac-
teristics of the USB configuration. The two-engine USB model of reference 6
with the Coanda plate deflected 55° is used for the following study. The
final method chosen as best for this configuration is then applied to other
configurations, and the predicted results compared with experiment where
possible.

Nacelles and thrust effects.- The engine nacelles on a typical USB
configuration (like that of ref. 6) extend back over the top surface of
the wing, effectively covering a portion of the wing. The present flow
model does not include induced effects from the nacelles nor loading on
the nacelles. The wing in the region covered by the nacelles is handled
as if there were no nacelles present (fig. 7). The jets start at the
nacelle inlet.[1] They induce flow on the wing in the nacelle region and
cause large wing loadings at that point. This effect is illustrated in
figure 10 on a two-engine USB model with a thrust coefficient of 0.95.
The higher predicted lift curve corresponds to the full loading on the
wing, including the jet-induced effects in the nacelle region of the wing.
The lower curve was obtained by neglecting the jet-induced velocities in
the loading calculation on the nacelle region of the wing (shown shaded in
fig. 7). There is a large reduction in the total lift on the wing, but
the effect on pitching moment is small because the portion of the wing
losing lift is close to the moment center. Note that the shaded area in
figure 7 only approximates the wing area covered by the nacelle. Since
complete vortex-lattice panels must be used, a better approximation of the
nacelle area can be obtained only by increasing the number of panels in
the region of interest. This was not possible in the present calculation
because of a limit imposed by the program on the total number of panels
used to describe the lifting surfaces.

The dashed curves in figure 10 show the effect of including the thrust
component in the lift direction and the contribution of the thrust to the
pitching moment caused by the location of the thrust axis above the moment
center. Inclusion of the thrust component, $C_J \sin \alpha$, increases the predicted
lift curve slope and improves the agreement between experiment and theory.
The thrust correction applied to the predicted pitching-moment curve moves
it in the direction of improved agreement between experiment and theory.

---

[1] This is done to obtain the proper ingestion rate at the nacelle exit.
Reference 1 has a discussion on this point.

The above comparisons indicate that the jet-induced velocities in the nacelle region on the wing should be neglected when computing the wing loading with jet interference, and the thrust component of the lift and pitching moment should be included in the predicted coefficients. Unless otherwise noted, all the following results are computed in this manner.

Jet height effect.- In the discussion of the jet model, it was noted that the steep axial velocity gradient near the jet boundary could cause large variations in the computed wing loading in the vicinity of the jet. The effect of the relative position of the jet boundary and the lifting surface was investigated for the present case. The predicted lift and pitching-moment coefficients for two jet heights are compared with experimental curves in figure 11. The solid curve was obtained with the jet boundary tangent to the wing and flap surfaces and the dashed curve was obtained with the jet raised 10 percent of its initial radius above the lifting surfaces. Based on the comparison with the lift curve, the tangent jet produces better agreement than the raised jet. The circulation distribution on the lifting surfaces is nearly the same for both wings, but the forces on the lifting surfaces are different because of the differences in the jet-induced axial velocity distribution.

Comparison of the two predicted pitching-moment curves illustrates that the largest reduction in the forces on the wing and flap surfaces generally occurs on the wing. This is shown as an increase in the nose-down pitching moment as the jet is raised.

Based on the above observations, the best model of the jet is one which is tangent to the lifting surface. In the results presented in the remainder of this report, the jet is placed tangent to the wing and flap surfaces unless stated otherwise.

Jet spreading rate.- The jet model requires that the growth of the jet cross-sectional area or the spreading rate be specified. Since the typical rectangular shaped jets are being modeled by multiple axisymmetric jets, it is desirable that the effect of the chosen spreading rate on the predicted aerodynamic characteristics be investigated. Spreading rates for coflowing rectangular jets are unavailable at the present time; therefore, the axisymmetric spreading rates in figure 4 are applied to each jet in the flow model. Predicted lift and pitching-moment curves corresponding

to several spreading rates are compared with experimental results in figure 12. According to the predicted jet velocity ratio, $V_J/V = 8.7$, the spreading rate curve associated with $m = 0.1$ in figure 4 is appropriate. This curve is shown as the long dash line in figure 12. The effects of more or less jet spreading (corresponding to $m = 0$ and 0.2 in fig. 4) are also shown in figure 12.

The trend is for the lift to decrease as the expansion rate decreases. A decreased expansion rate implies a decrease of mass entrained into the jet. The lower the entrainment, the lower the induced upwash field on the wing in the vicinity of the jet; thus, the lower the circulation on the wing. These particular results tend to show that one could tailor the expansion rate as a function of angle of attack to improve the agreement. For example, $m = 0.2$ when $\alpha < 4^{\circ}$ and $m = 0.1$ when $\alpha > 4^{\circ}$ would give excellent agreement in figure 12. However, too little is known about the expansion of rectangular jets to justify using such a procedure at the present time. In the results that follow, the jet spreading rate will be specified by the jet velocity ratio and that spreading rate will be used throughout the angle-of-attack range.

Jet separation effect.- All results presented thus far have been calculated assuming the jet to be attached to the wing and flap upper surfaces from the engine exit nozzle to the trailing edge of the flap or Coanda plate. The combined jet and lifting-surface models have the capability of simulating a condition in which the jet-wake separates from the flap ahead of the flap trailing edge. The effect on the predicted aerodynamic characteristics of allowing the jet to separate from the Coanda plate of the USB model in reference 6 is shown in figure 13. For illustrative purposes, the jet is assumed to separate from the aft 30 percent of the Coanda plate. At the separation point, the jet leaves the flap surface tangent to it as shown in the sketch in figure 13. The fully attached result is shown as the solid curve, and the simulated separation result is presented as a dashed curve. Allowing the jet to separate from the flap causes a reduction in the predicted lift of about 15 percent. The pitching-moment curve indicates that most of this lift is lost from the flap as there is a large nose-up moment produced by the jet separation effect.

22

These results are presented more to illustrate some interesting effects and potential uses of the method than to suggest that jet separation should be considered as part of the prediction procedure. The vortex-lattice, lifting-surface scheme is a potential method that presumes attached flow everywhere on the wing and flaps. It is more likely that separation on USB configurations would occur on regions of the wing and flaps not directly influenced by the jet. Thus, in the results presented hereafter, the jet is assumed to be attached to the wing and flap from the engine exit to the trailing edge, and the jet leaves the trailing edge of the flap tangent to it.

Predicted Aerodynamic Characteristics

In the previous section, the effects of various parameters on the predicted longitudinal aerodynamic characteristics on a two-engine USB configuration with one flap angle and one thrust coefficient were examined. Based on these results, the following calculation procedure was developed. The rectangular shaped jet is modeled by a series of circular jets with a minimum of overlapping initially. The jet centerlines move aft at constant semispan locations which are aligned with wing and flap lattice panel control points. The individual jet expansion rate is chosen from the axisymmetric curves in figure 4 based on the jet velocity ratio. The jets are positioned such that they are tangent to the wing and flap sur-faces; and upon leaving the trailing edge of the last flap, the jet is allowed to return to the free-stream direction in a distance of approxi-mately one wing chord. The jet-induced velocities in the region of the wing shielded by the nacelles are omitted from the interference calculation, and the thrust force contribution to lift and pitching moment is included.

The above procedure is now applied to three different USB configura-tions with a range of thrust coefficients and flap angles. Configurations with both two and four engines are considered, and comparisons with data are made where possible.

Two-engine configuration.- The first USB model to be considered is the two-engine configuration of reference 6. The vortex-lattice layout is shown in figure 7 as is the approximate nacelle position. The rectan-gular jet is modeled by four circular jets as described previously. The flap immediately aft of the engine in the region $0.11 \leq \eta \leq 0.43$ is a Coanda plate which is modeled by the vortex lattice as three separate

flaps with no gaps between them for purposes of numerical accuracy. Outboard of the Coanda plate is a double-slotted flap which has a total deflection somewhat less than that of the Coanda plate; and outboard of the double-slotted flaps, $\eta > 0.75$, is an aileron with a constant $20°$ deflection angle. The exact geometry is presented in greater detail in reference 6.

Measured (tail-off) and predicted lift and pitching-moment coefficients on the above model with Coanda plate deflected $30°$ are compared in figure 14(a). The power-off and $C_J = 0.54$ and 1.08 lift curves are in good agreement, although the predicted lift curve slope is lower than that measured. The actual agreement between the measured and predicted lift is best in the range $8° \leq \alpha \leq 20°$, as the predicted lift is always too high near $\alpha = 0°$. As the thrust coefficient is increased, the lift tends to be overpredicted; and at the highest thrust coefficient, $C_J = 2.33$, the agreement between experiment and theory is poor.

The pitching-moment coefficient on the same figure show reasonably good agreement between experiment and theory for the power-off and $C_J = 0.54$ conditions. As power is increased, the agreement deteriorates rapidly. If the measured pitching-moment curves are taken as an indicator of the type of lift distribution, it can be seen that as thrust is increased the associated additional loading occurs on the flap. This is not the case in the prediction method. The gross additional loading may be predicted well, but it appears to be evenly distributed over the wing and flap so as not to change the pitching-moment coefficients; or as is the case in figure 14(a), most of the additional interference loading is concentrated on the wing causing a nose-up pitching moment.

The forces and moments due to the fuselage and nacelles are neglected in this calculation. Though the missing normal force may be small, the pitching moment could have a considerable effect on these results. There is also a possibility that jet interaction with the fuselage aft of the wing could contribute to the configuration forces and moments. The present method is unable to account for interactions of this type.

The span-load distributions on this two-engine model at $\alpha = 0°$ and $24°$ are shown in figures 14(b) and (c), respectively. The span loading on the wing is shown in the lower portion of each figure and that on the Coanda plate is shown in the upper part of the figure. The loading on the

24

outboard flaps is small and is not presented on these figures. The effect of the engine wake is obvious on these curves as there is a dramatic increase in the wing and flap loading in the vicinity of the wake. The roughness in the loading distribution is caused by both the jet model and the vortex-lattice arrangement. Use of multiple circular jets to represent a single rectangular jet poses some numerical problems and results in an induced velocity distribution on the wing surface which is not as smooth as desired. If a finer lattice arrangement were used, the loading gradients between lattice panels would be smaller and result in a smoother spanwise variation in loading.

Comparing figures 14(b) and (c), it is interesting to note that the wing loading increases a large amount with angle of attack, but the flap loading does not. This is true with power on or power off. The wing-flap interference characteristics in the vortex-lattice method cause this effect. For example, if the wing loading increases, the induced downwash at the flap position increases and tends to reduce the flap loading. An increase in the flap loading increases the upwash on the wing and increases its loading. Thus, we have the effects of the engine wake increasing the loading on both the wing and flap, the increased loading on the flap tending to increase the wing loading even more, and the increased wing loading tending to decrease the flap loading. The net effect is as shown.

Similar comparisons on the same two-engine USB model with the Coanda plate deflected 55° are shown in figure 15. The power-off and $C_J = 1.08$ lift curves in figure 15(a) are in reasonably good agreement with experiment; but as thrust is increased to $C_J = 2.03$, the predicted lift curve is too high by approximately 10 percent at $\alpha = 0^\circ$. The pitching-moment curves are similar to those obtained for the lower flap angle with the exception that the power-off pitching moment is not in as good agreement for this higher flap angle. The span-load coefficients in figure 15(b) for the configuration at 24° angle of attack have the same appearance as those calculated for the lower flap angle. This is to be expected as the jet model and the vortex-lattice arrangement are the same for all flap angles for this two-engine configuration.

Similar results on the same two-engine configuration with the Coanda plate deflected 75° are presented in figure 16. For power off, the predicted lift curve is approximately 20 percent higher than the measured

curve at $\alpha = 0°$. This difference is possibly due to flow separation occurring on this model. With power on, the predicted lift curve is in good agreement with experiment at $C_J \simeq 1$, and as in the previous comparisons for lower flap angles, the lift curve is too high at $C_J \approx 2$. The measured and predicted pitching-moment curves have the same relative appearance as those at the 55° flap angle in figure 15.

The predicted span-load distribution at $\alpha = 24°$ is shown in figure 16(b). Since the jet model and the wing-flap model are basically the same at this flap angle as they were at lower flap angles, the resulting span loadings have an appearance similar to those discussed earlier.

Four-engine configuration.- Comparisons were also made for the four-engine USB model of reference 7. This model has basically the same wing as the previous two-engine model; the major difference being the larger Coanda plate. The vortex-lattice arrangement for this wing is shown in figure 17. Each rectangular jet is modeled by four circular jets located as shown in the sketch. The Coanda plate aft of the engine covers the region $0.11 \leq \eta \leq 0.70$, and it is modeled by three separate flaps with no gaps between them. The fourth flap shown in figure 17 is added to obtain the 90° flap deflection configuration. The aileron outboard of $\eta = 0.70$ has a constant 20° deflection angle. Leading-edge blowing for purposes of boundary-layer control was applied during the power-on tests.

Measured and predicted aerodynamic characteristics on the above model with Coanda plate deflected 30° are shown in figure 18. The lift curves in figure 18(a) are in good agreement with experiment for thrust coefficients of one or less. As was the case with the two-engine comparisons in figure 14(a), the predicted lift curves are too high for thrust coefficients of 2.0 or greater. The character of these predicted lift curves is similar to the two-engine results in that the lift coefficient is generally too high at zero degrees angle of attack and the lift curve slope is slightly lower than the experimental value.

The pitching-moment coefficients are different than the typical results obtained on the two-engine model. As before, the predicted slopes

are too low but the predicted pitching moments here are too nose-down at all thrust coefficients. The four-engine theoretical model develops more lift on the flaps, with respect to that developed on the wing, than does the similar two-engine model. In particular, at high angles of attack, the predicted lift on the flaps is too large. The differences between figures 14(a) and 18(a) may be due to the limited ability of the present method to simulate experimental effects, in particular, effects of jet spreading and mixing between the jets.

The predicted span-load distributions on this four-engine model at $\alpha = 24^\circ$ are shown in figure 18(b). The span loading on the wing is shown in the lower figure and that on the Coanda plate is shown in the upper figure. As before, the loading on the aileron is not shown. The engine-wake effects are easily distinguished on these curves. The restriction imposed on the lateral motion of the jet wakes is the major reason that the inboard and outboard engine effects are separated on both the wing and flap. If a rectangular shaped jet model were used, which would allow the jets to merge, the loading on the flap would not exhibit the large dip between the wakes, and the predicted loading would have a more continuous spanwise distribution.

Figure 19 shows the results for the same four-engine configuration with the Coanda plate extended to 90° as shown in figure 17. The power-off results, figure 19(a), denoted as attached flow in the figure, are approximately 25 percent high, a result similar to that shown for the 75° flap angle on the two-engine configuration in figure 16. Anticipating the possibility that separation was occurring on the Coanda plate extension which was at a 90° angle to the wing chord line, the extension was removed from the vortex-lattice model. The results obtained on this modified configuration are denoted as "separated flow" in figure 19(a). It is interesting that this latter result is in good agreement with the data. In reality, partial flow separation probably occurred over more of the Coanda plate than just the extension; and it is likely that some separation could have occurred near the wing leading edge, a phenomena which cannot be modeled by a vortex-lattice approach. The pitching-moment curves corresponding to the two lift curves exhibit more nose-down moment than does the data, but the curve corresponding to the modified Coanda plate is adjusted in the direction of better agreement.

27

When power effects are added to the calculation, the predicted lift curves are again too high; and the pitching-moment curves have more nose-down sense than the data. The full Coanda plate was used for these calculations. If these results are compared with the two-engine results for the 75° flap in figure 16, some interesting comparisons can be made. The four-engine lift data are much closer to the predicted potential lift than the two-engine data. We can infer from this that more of the wing and flaps are encountering attached flow on the four-engine model than on the two-engine model. The two-engine model Coanda plate extends over about 40 percent of the semispan and the four-engine model Coanda plate extends over nearly 70 percent of the semispan; therefore, the four-engine model has less trailing-edge flap susceptible to flow separation.

The predicted span-load distribution is shown in figure 19(b). Because of the similarity of the jet models, these results have the same form in those presented in figure 18 for the lower flap angle.

LRC four-engine configuration.- A second four-engine USB model (ref. 8) was chosen for additional comparisons with experiment. The model has a simple body-of-revolution fuselage and a high wing with two tip jet-driven ducted fans in a siamese pod attached to the wing upper surface. The wing quarter chord is swept 25°, and full-span trailing-edge flaps with provision for spanwise variation of deflection angles are utilized. The fan exhausts were directed at the wing upper surface through rectangular nozzles. The model used boundary-layer control (BLC) to try to maintain attached flow over the outboard portions of the trailing-edge flaps during all tests, power on and power off.

The high-aspect-ratio rectangular engine exit is modeled by eight adjacent circular jets. There is a small gap between the inboard four jets and the outboard four jets to allow the jet model to better cover the span of the wing. This gives the jets a similar appearance to those on the previous four-engine model. The lattice arrangement is shown in figure 20.

The measured and predicted lift and pitching-moment curves are compared in figure 21 for a uniform trailing-edge flap deflection angle of 30°. Data are presented for two levels of BLC blowing, and there is a noticeable effect due to the quantity of blowing. No attempt was made to predict the BLC effect. The predicted lift curves are in good agreement with the measured results for all power conditions. As is typically the case with

28

the predicted results, the lift tends toward the high side of the data at
the highest thrust coefficients. Pitching-moment comparisons made in this
same figure are in poor agreement. The predicted moment curves have the
same character as those in previous four-engine results; however, the data
presents itself in an entirely different manner. The measured pitching
moments show larger variations with lift coefficient, angle of attack, and
thrust coefficient than do the results on other wings.

CONCLUDING REMARKS

The purpose of the investigation reported herein was to assess the
capability of an existing EBF prediction method to calculate the lift and
pitching moment of USB configurations. Comparison between measured and
predicted aerodynamic characteristics were used to evaluate the calculation
procedure. An evaluation of the method, its shortcomings, possible areas
of improvement, and specific recommendations for improvements are discussed
in this section.

The vortex-lattice, lifting-surface method has been applied to wing-flap
configurations with and without power effects in this work and in refer-
ence 1. Its success under power-off conditions for moderate flap angles
has been demonstrated for a wide range of configurations. It is reliable
for lift prediction so long as no separation occurs on the wing or flaps;
however, its success in pitching-moment prediction is more limited. As
described in reference 1, the accuracy of the pitching-moment results
obtained from the vortex-lattice method is dependent on a number of geo-
metric characteristics such as wing sweep, flap angle, and lattice arrange-
ment. The effect of the latter item is evaluated in great detail in
reference 1, and the guidelines set up in that report were applied where
possible in the present work. The effect of wing sweep on pitching-moment
coefficients illustrated in reference 1 indicates that as wing sweep
increases, the quality of the predicted pitching moments generally
decreases. This is caused in part by inaccuracy in the prediction of the
distribution of loading on the swept flap. Since the outboard section of
a typical swept flap lies a considerable distance behind the moment center,
small changes in the distribution of lift near the tip can have a large
effect on the associated pitching-moment coefficients.

The vortex ring jet-wake model was shown to be capable of matching measured mass and momentum of a single circular jet (ref. 1). The modeling of a rectangular jet by a number of adjacent circular jets, as was done in the present work, has not been verified by comparison with experimental jet flow field data. Since the jet momentum is calculated from a measured thrust coefficient, it can be assumed that the initial momentum in the jet model is correct. What is still unknown is how well the mass in the jet model matches the actual jet. This is a measure of how well the entrainment in the analytical model matches the entrainment in the actual jet and thus how well the induced flow field in the vicinity of the jet boundary is approximated. The answer to this question depends on the availability of experimental data on the mass flow in coflowing rectangular jets. The authors have been unable to find data of this type which can be used to evaluate the jet model. In the current method, the entrainment of each of the circular jets is specified by the expansion rate of the jet, and the expansion rate is chosen from axisymmetric jet information. This procedure has proven successful in predicting the gross lift characteristics and lift increments due to jet interference; therefore, the jet flow field in the vicinity of the wing must be approximately correct.

The parametric study of individual jet expansion rate (fig. 12) on lift showed a small total effect, but the magnitude of the incremental effect is large compared to the difference between predicted and measured lift curves. These results also pointed out that if the chosen jet expansion rate is allowed to vary as a function of angle of attack in the appropriate manner, the predicted lift curve slope can be changed to enchance the agreement between experiment and theory. However, there is no rational or empirical basis for changing the expansion rate with angle of attack at this time.

The forces and moments on and induced by the engine nacelles and the fuselage are neglected in the current study. As was shown in figure 10, some provision must be made in the wing loading calculation to correct for wing lift and jet interference effects in the region of the nacelles. The corrective methods used in the calculations described in this report are only approximate, and better procedures of including nacelle and fuselage interference effects need to be developed.

The effect of lateral motion of the jet is not investigated in this study because of the problem discussed earlier regarding the void regions between the individual circular jets. If the jets are allowed to move in a spanwise direction, the vortex-lattice control points will fall inside these void regions and an incorrect local loading will be predicted. This difficulty would disappear if a rectangular shaped jet model were used in place of the multiple circular jets. This could have an effect on the pitching moment, particularly for swept wings, because spanwise movement of the rectangular jet would allow the span loading to be shifted outboard.

A fringe benefit of using a rectangular shaped jet model in the calculations is the reduced cost of computation. The multiple circular jet scheme uses a minimum of four individual jets to model a single rectangular jet. Thus, the part of the calculation time devoted to computing jet-induced velocities could be reduced by 75 percent if a single rectangular jet is used. The time-saving benefit is greatly increased if higher aspect ratio jets requiring more than four circular jets are considered.

With regard to an overall assessment, it appears that the approach embodied in reference 1 has considerable promise for predicting the aerodynamic characteristics of USB configurations. A combination of jet-wake and vortex-lattice models has provided a method which results in good agreement between measured and predicted lift over a range of geometric and flow parameters, but the method does not predict pitching moments with the same accuracy. A number of problem areas associated with differences between EBF and USB configurations have been identified, but means for solving these problems appear available. Consequently, it is felt that a successful USB engineering prediction method can be developed based on the approach of reference 1.

NIELSEN ENGINEERING & RESEARCH, INC.
        Mountain View, California
                April 1975

REFERENCES

1. Dillenius, M. F. E., Mendenhall, M. R., and Spangler, S. B.: Calculation of the Longitudinal Aerodynamic Characteristics of STOL Aircraft with Externally-Blown Jet-Augmented Flaps. NASA CR-2358, Feb. 1974.

2. Abramovich, G. N.: Theory of Turbulent Jets. MIT Press, 1963.

3. Sforza, P. M., Steiger, M. H., and Trentacoste, N.: Studies on Three-Dimensional Viscous Jets. AIAA Jour., vol. 4, no. 5, May 1966, pp. 800-806.

4. Trentacoste, N. and Sforza, P.: Further Experimental Results for Three-Dimensional Free Jets. AIAA Jour., vol. 5, no. 5, May 1967, pp. 885-891.

5. Perry, Boyd, III and Green, George C.: Wind Tunnel Investigation of Aerodynamic Loads on a Large-Scale Externally Blown Flap Model and Comparison with Theory. NASA TN D-7863, Mar. 1975.

6. Aoyagi, K., Falarski, M. D., and Koenig, D. G.: Wind-Tunnel Investigation of a Large-Scale Upper-Surface-Blown-Flap Transport Model Having Two Engines. NASA TM X-62,296, Aug. 1973.

7. Aoyagi, K., Falarski, M. D., and Koenig, D. G.: Wind Tunnel Investigation of a Large-Scale Upper Surface Blown-Flap Model Having Four Engines. NASA TM X-62,419, 1975.

8. Phelps, A. E., Letko, W., and Henderson, R. L.: Low-Speed Wind-Tunnel Investigation of a Semispan STOL Jet Transport Wing-Body With an Upper-Surface Blown Jet Flap. NASA TN D-7183, May 1973.

32
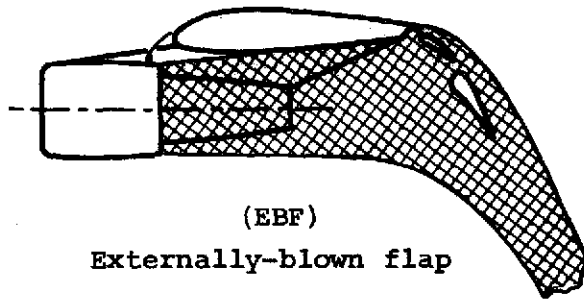
(EBF)
Externally-blown flap
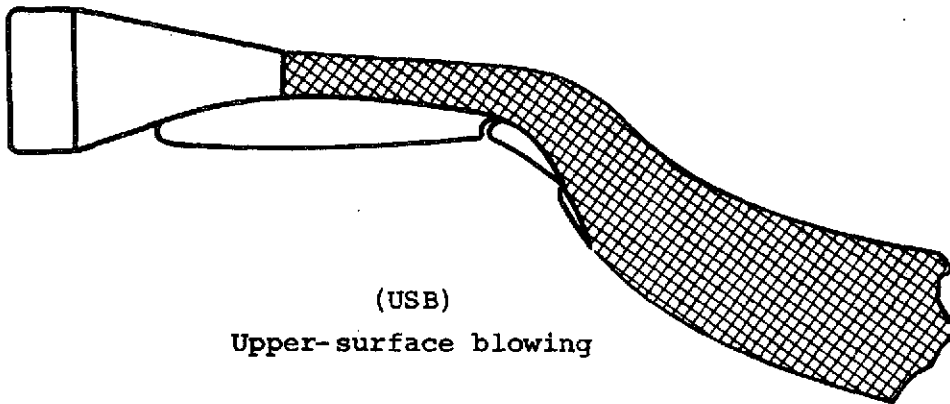
(USB)
Upper-surface blowing

Figure 1.- External flow, jet augmented,
high lift systems.
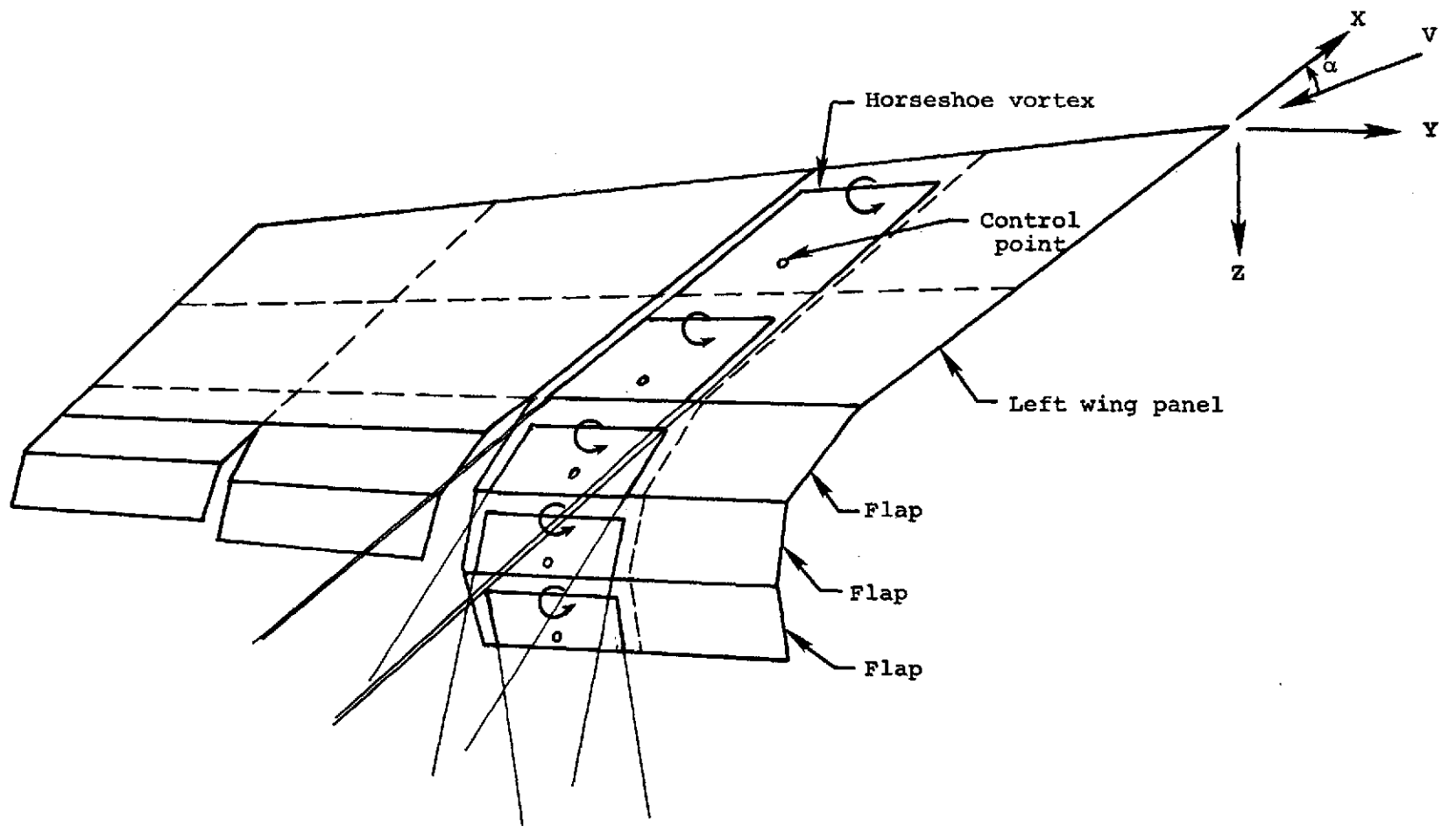
Figure 2.- Multiple flap vortex lattice arrangement.
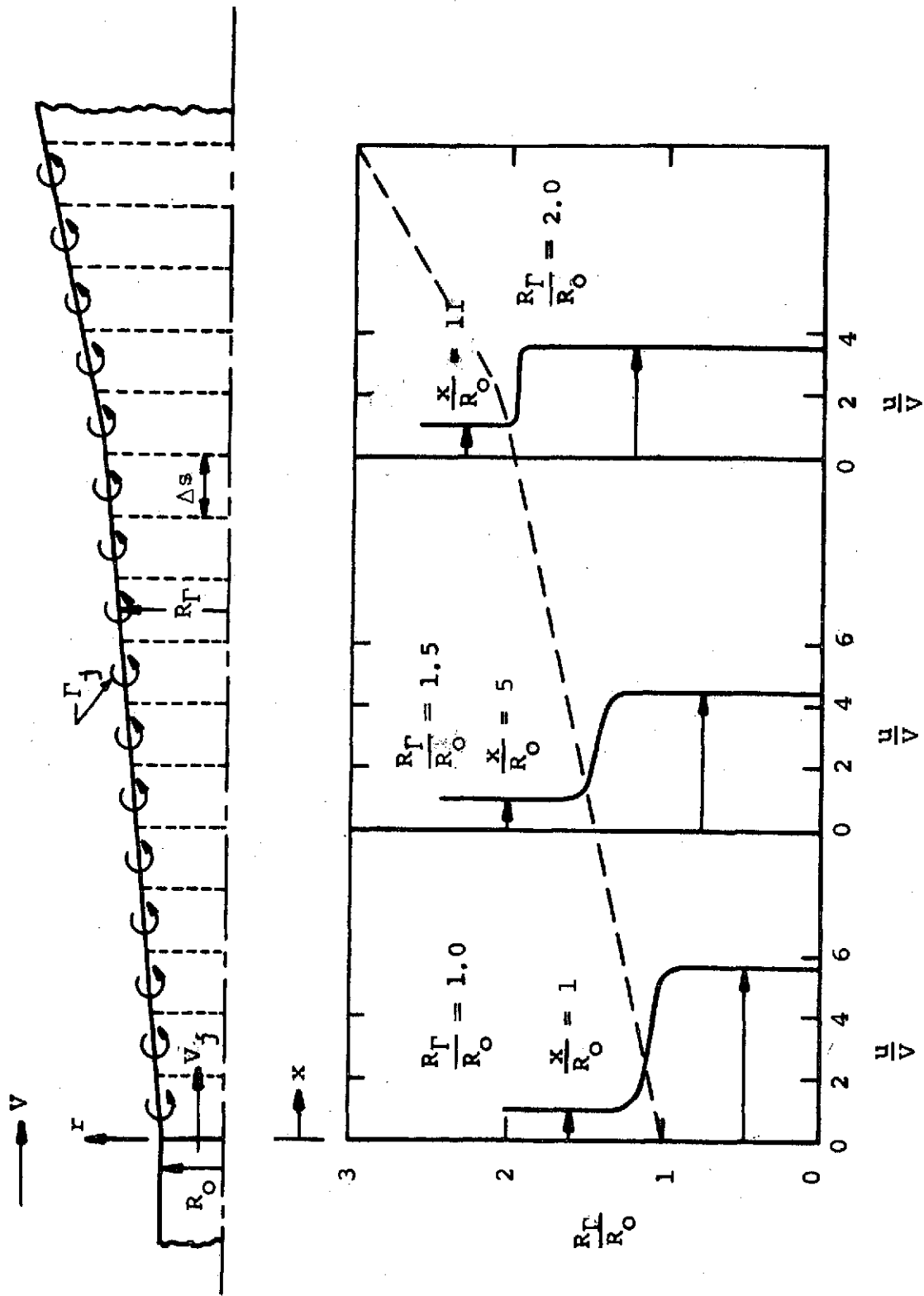
Figure 3.— Vortex ring wake model and velocity profiles for $V_j/V = 6$.
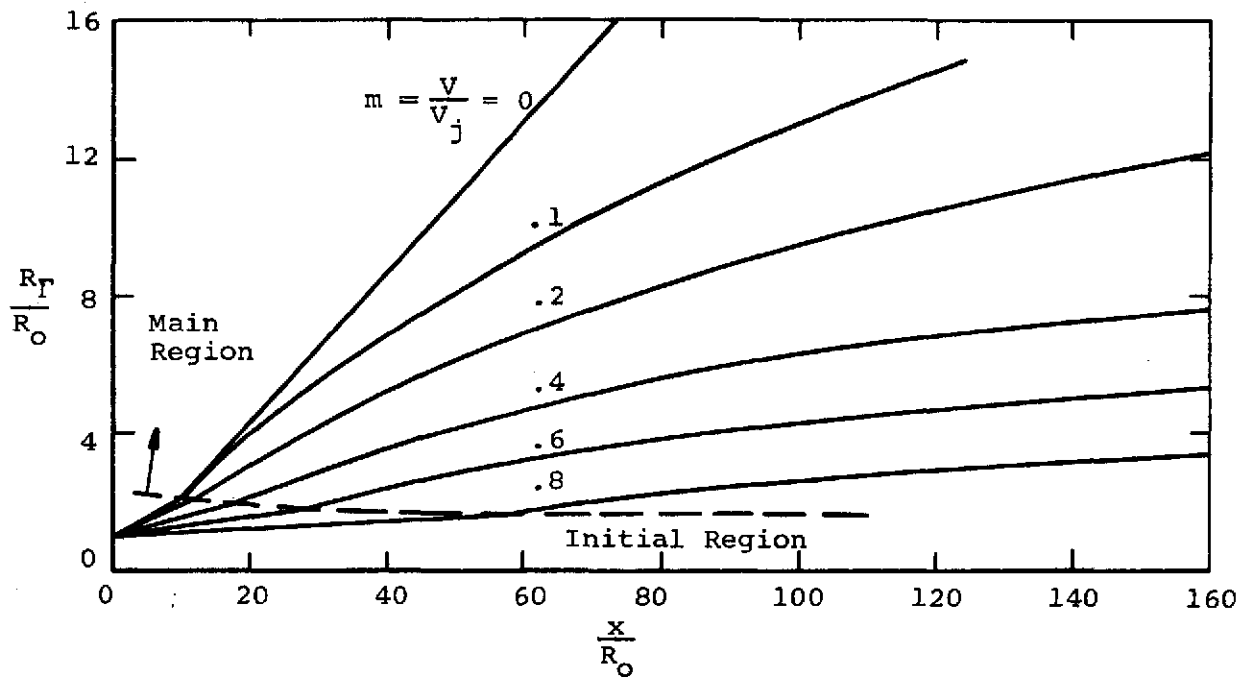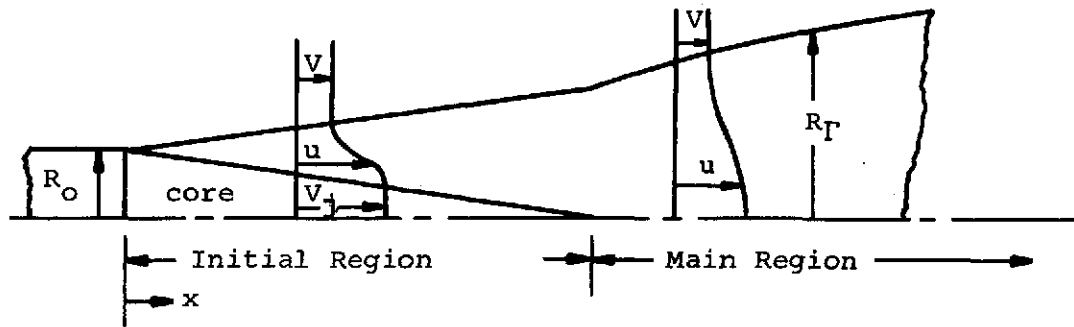
Figure 4.- Analytical spreading rate of an
axisymmetric jet in a coflowing stream.
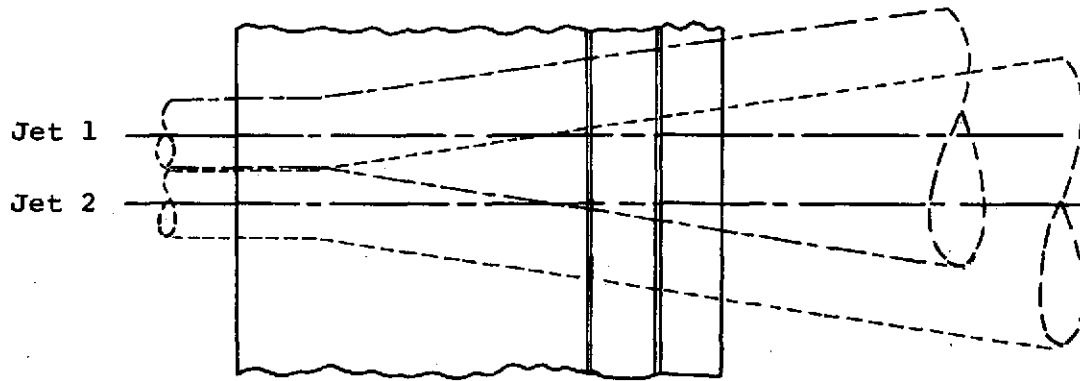
Top view
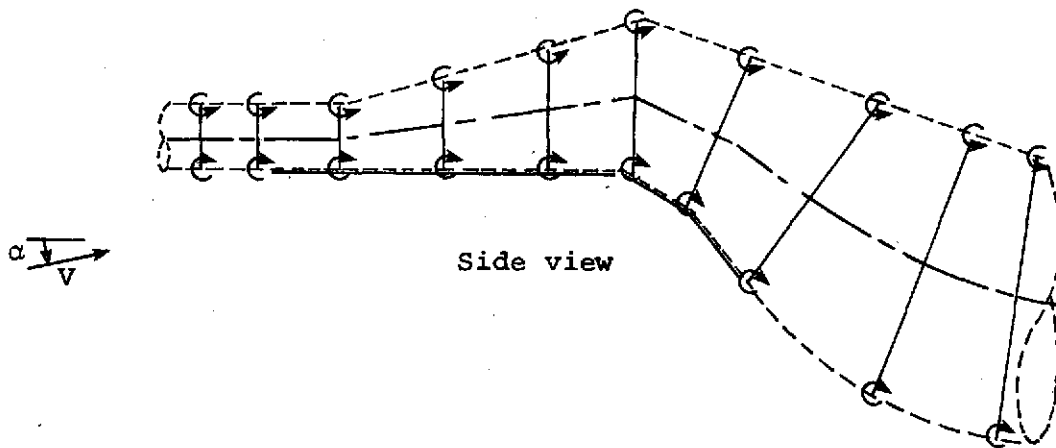
Side view

Figure 5.- Schematic representation of wing and flaps and jet wake models for an USB configuration.
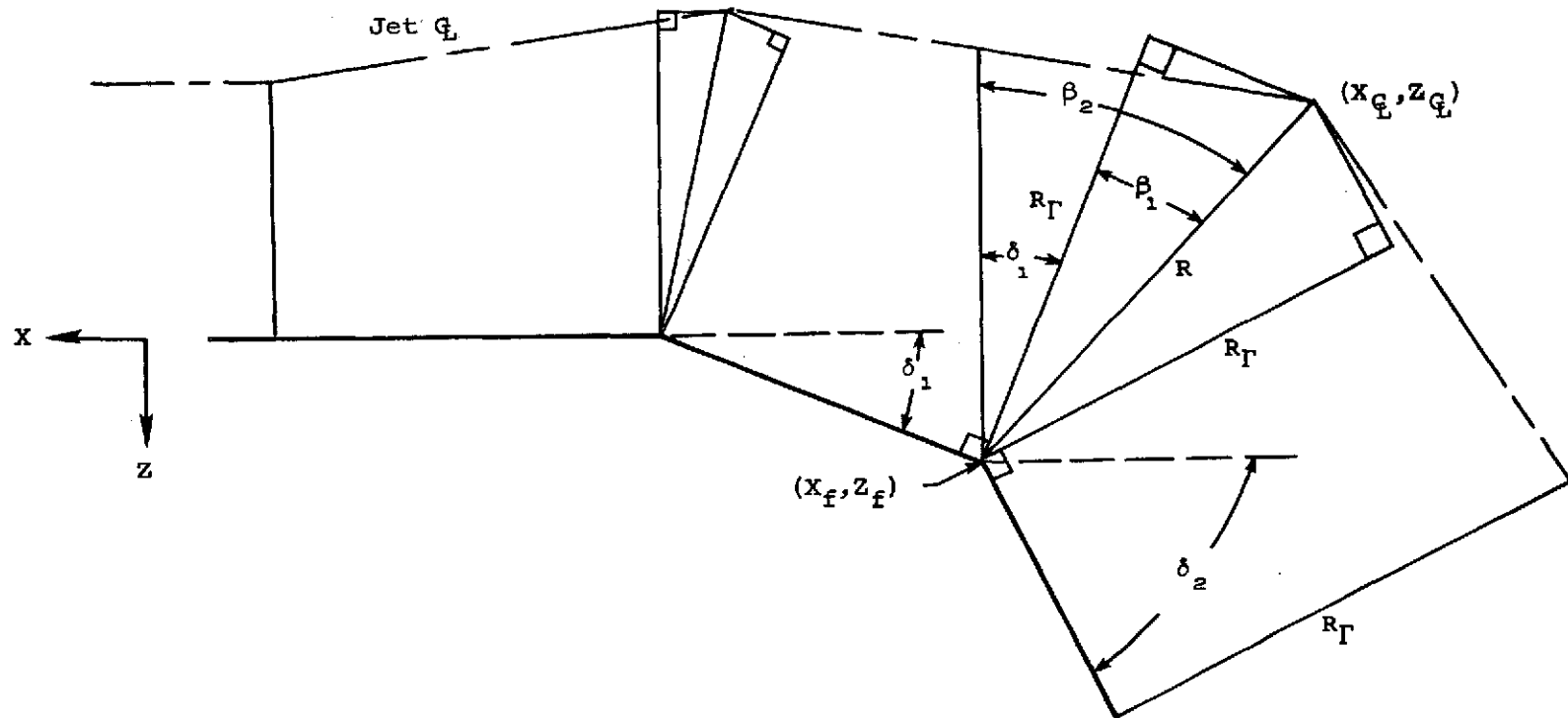
Figure 6.- Jet centerline specification method.

Nacelle
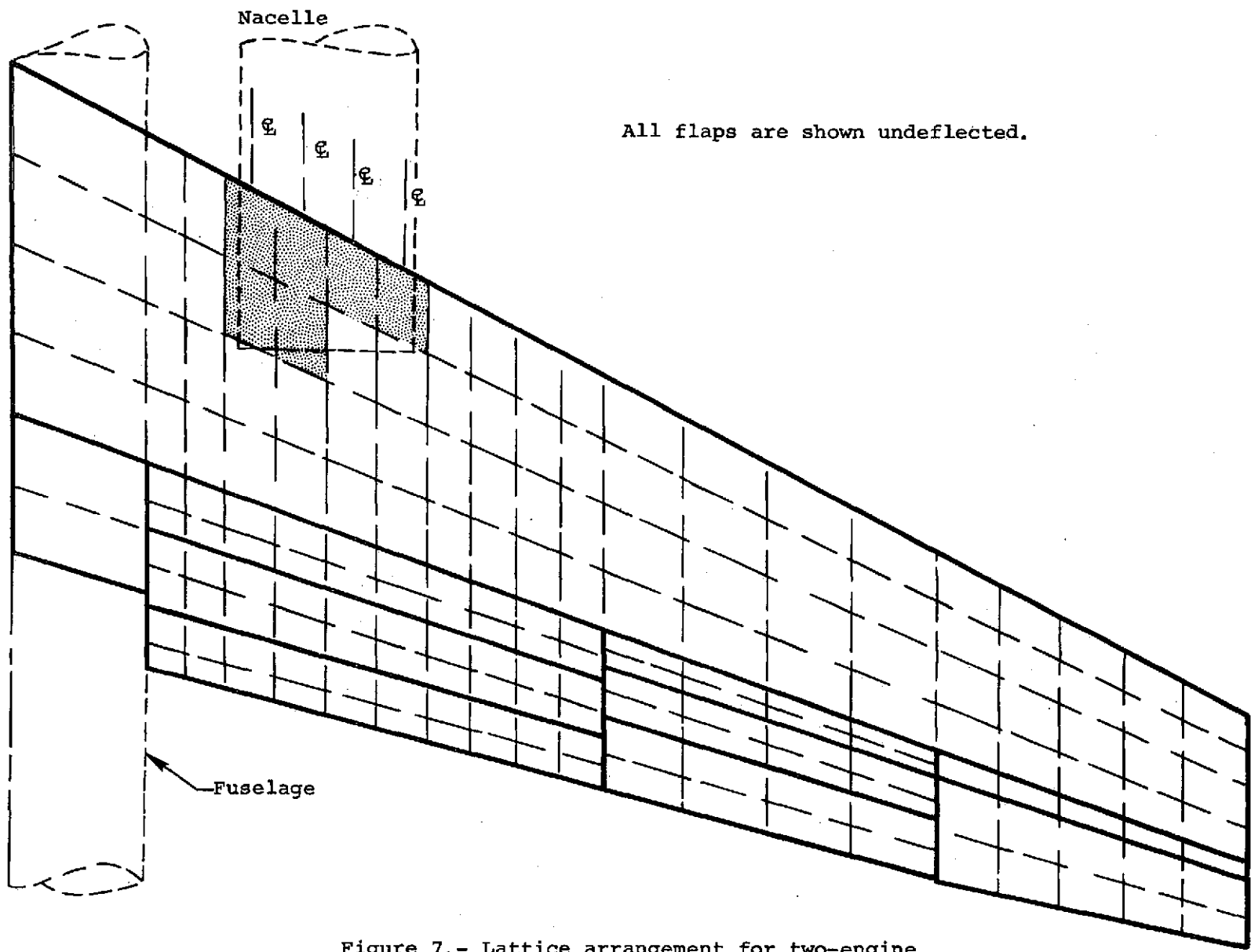
All flaps are shown undeflected.

Fuselage

Figure 7.- Lattice arrangement for two-engine
USB model of reference 6.
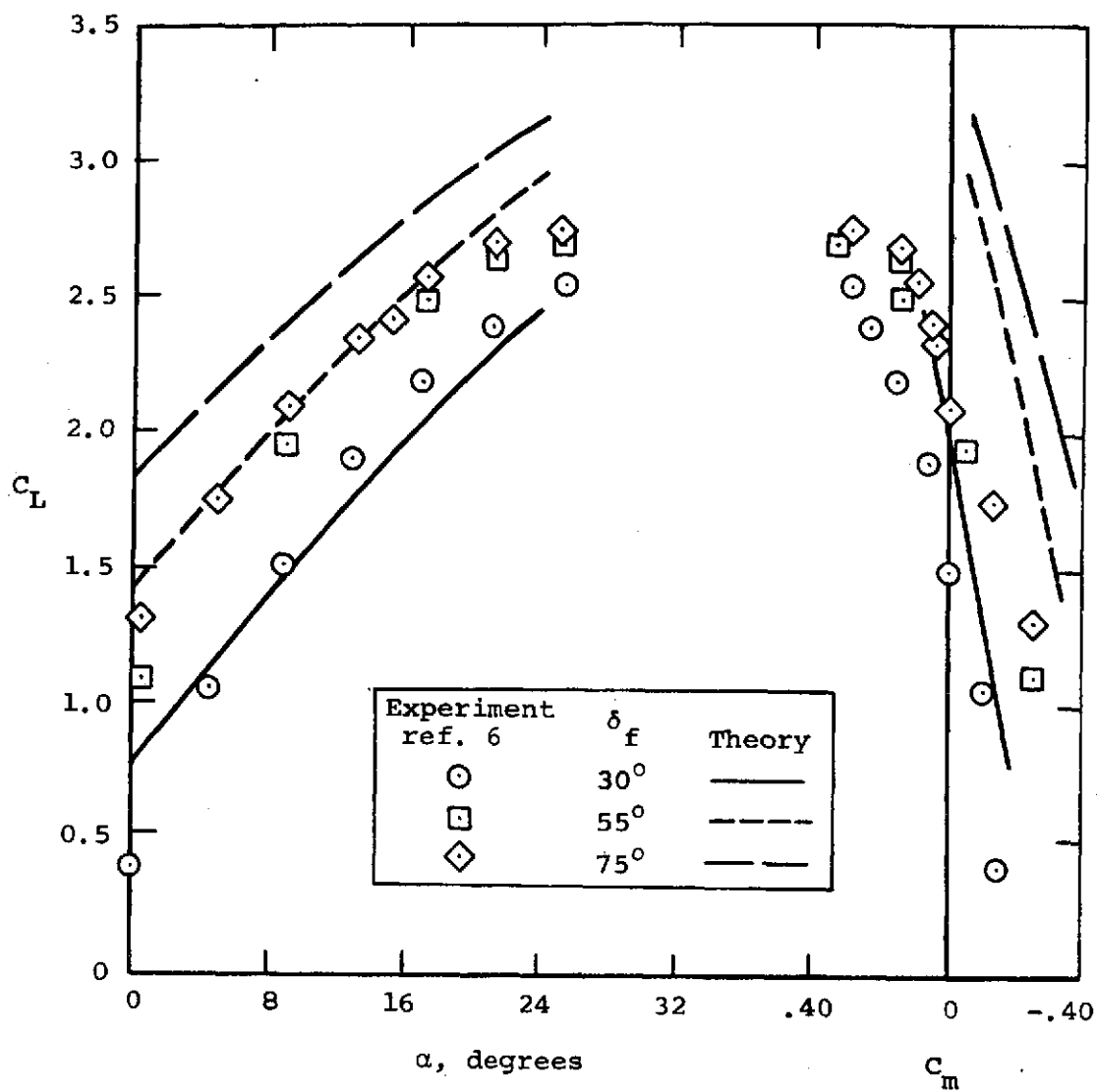
Figure 8.- Measured and predicted lift and pitching-moment
coefficients on a two-engine USB model,
tail off, $C_J = 0.0$.

Rectangular
Jet $\mathcal{C}_L$

2.64'

.39' .39' .39' .39'

.72'

Void
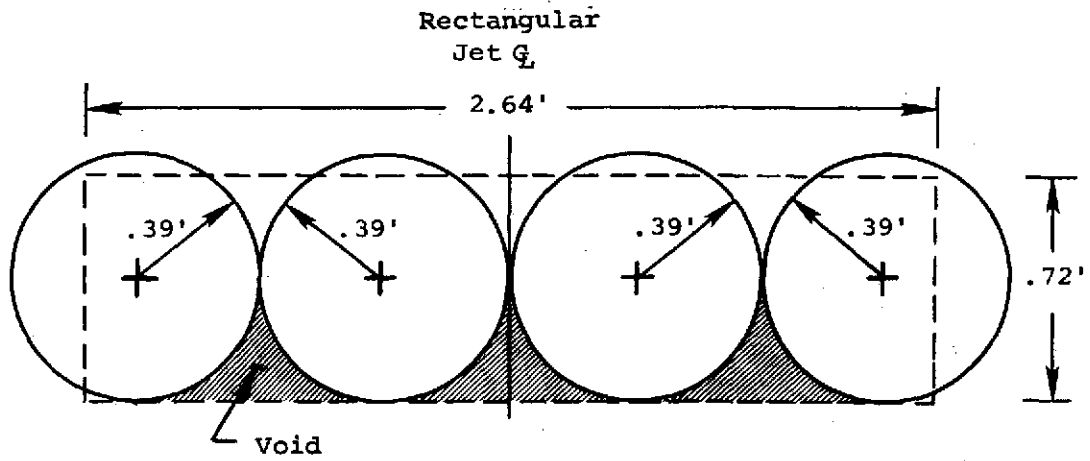
(a) Jet cross section at
engine exhaust nozzle.

Rectangular
Jet $\mathcal{C}_L$

Void   Wing upper surface
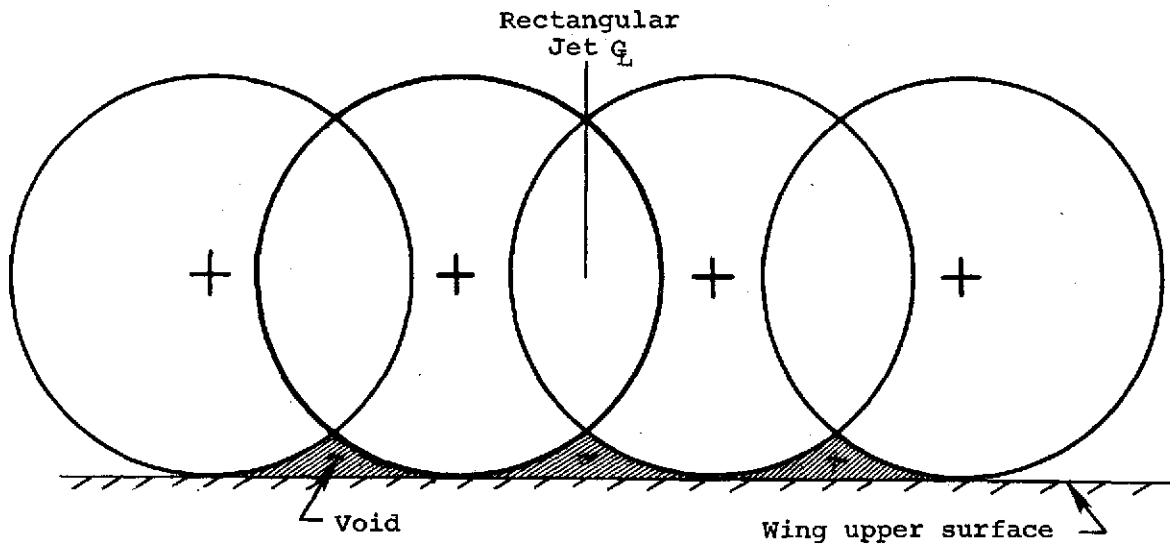
(b) Jet cross section 18 inches
aft of engine exit nozzle.

Figure 9.- Circular cross-section jet approximation
of a rectangular jet.

41

$T = 1{,}700$ lbs.

$V = 63$ ft/sec

$C_\mu = 3.5$

→ Outboard

Wing surface

$Y_{\mathcal{C_L}}$, inches

Induced upwash velocity on wing surface.

$\dfrac{w}{v}$

——— Jet model

— — — Average velocities from measured static profiles

Induced axial velocity at jet centerline

$\dfrac{u}{v}$

$Y_{\mathcal{C_L}}$, inches
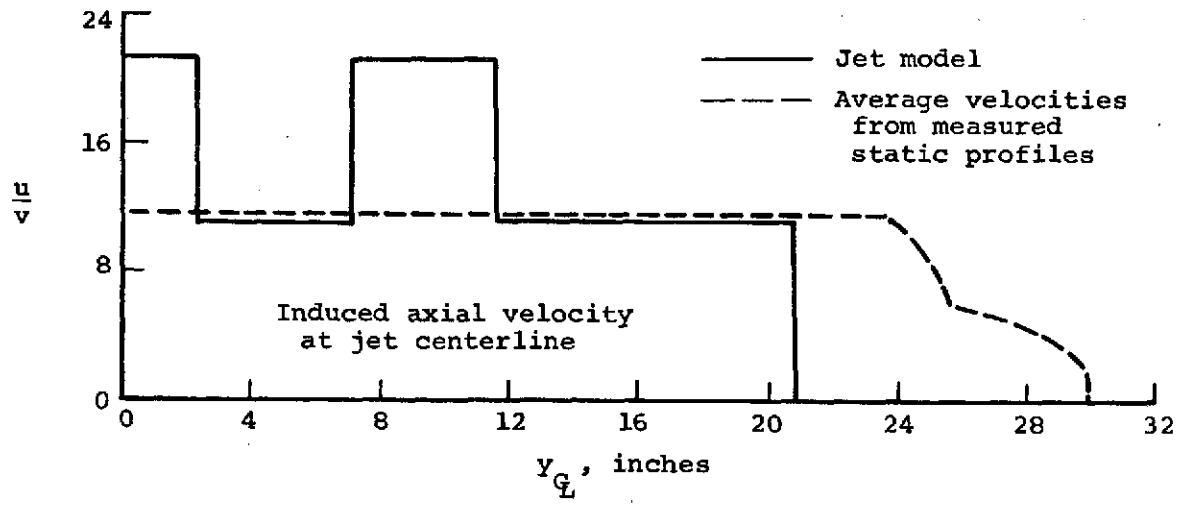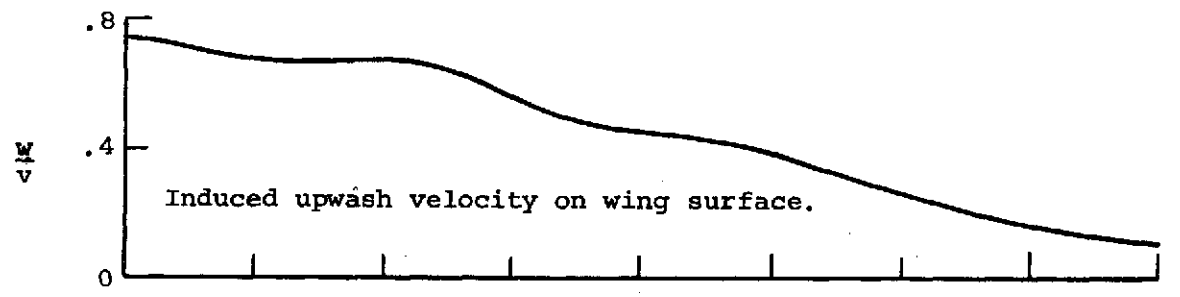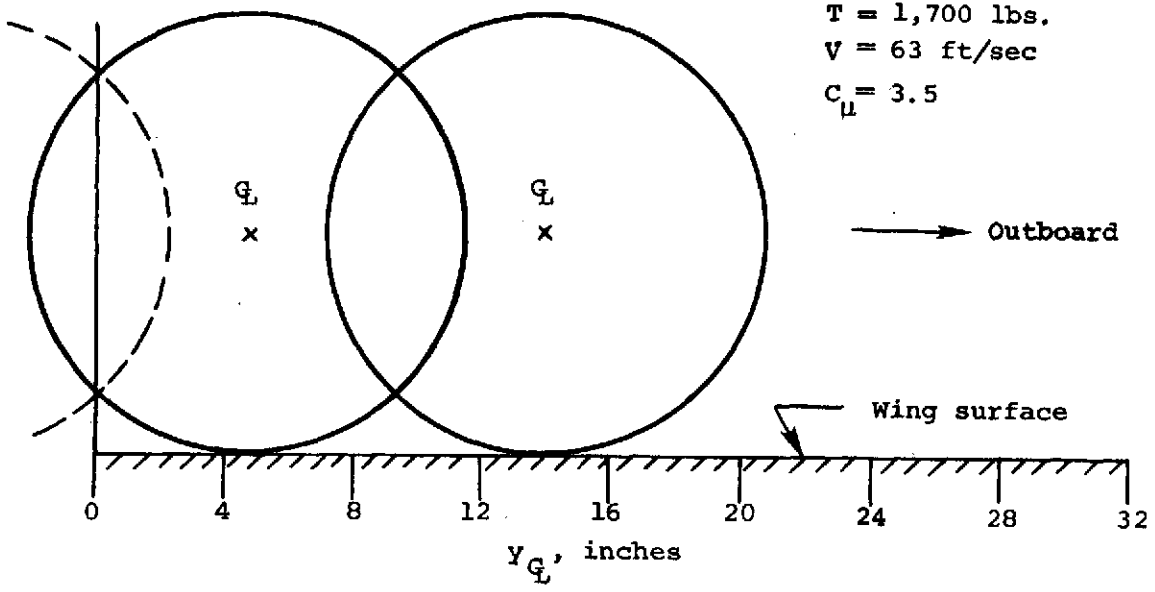
(c) Velocity field 18 inches aft of exhaust exit induced by jet model.

Figure 9.- Concluded.

42
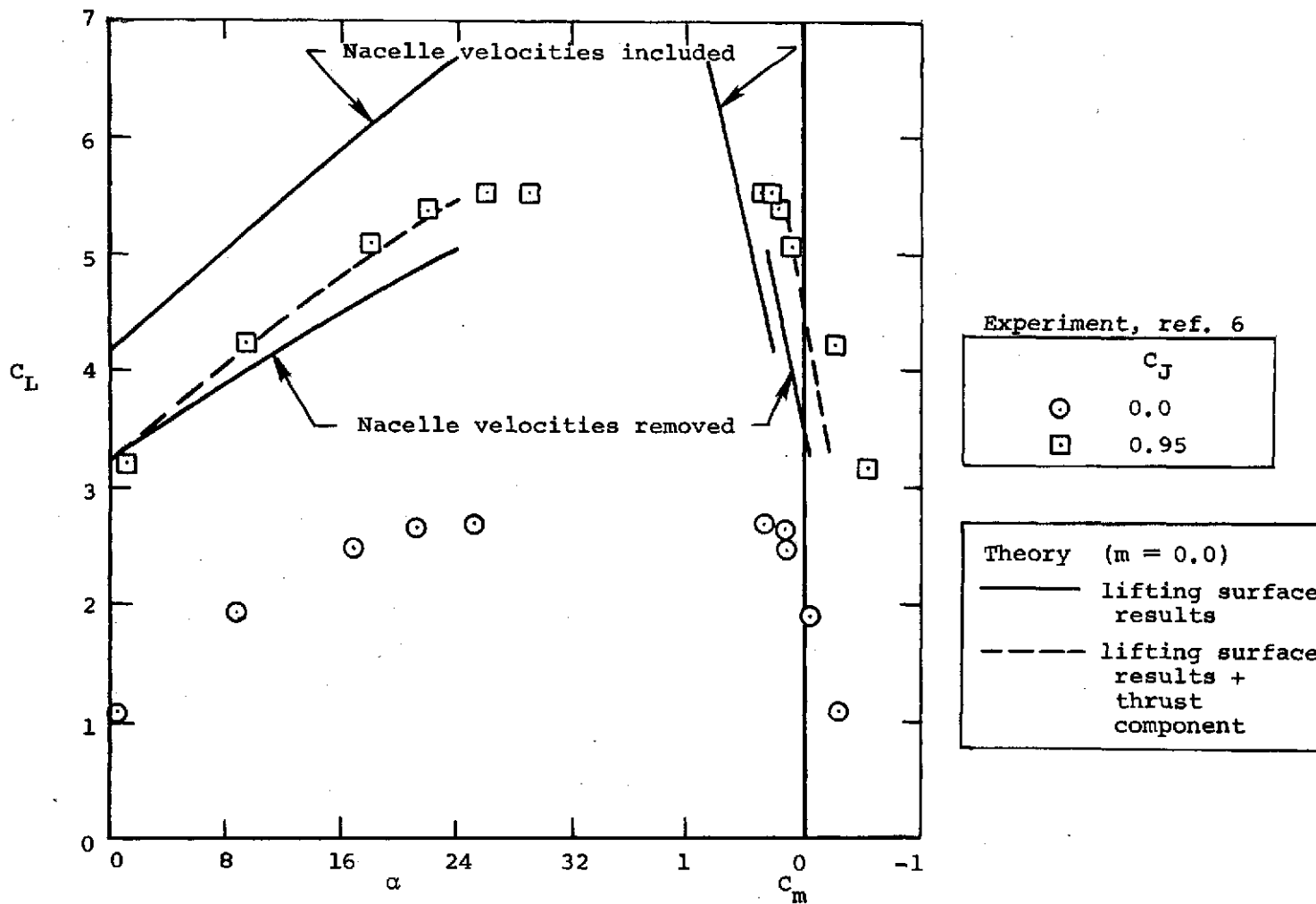
Figure 10.- Effect of wing loading in nacelle region on the predicted lift and pitching moment coefficients on a two-engine USB model, tail off, $\delta_f = 55^\circ$.
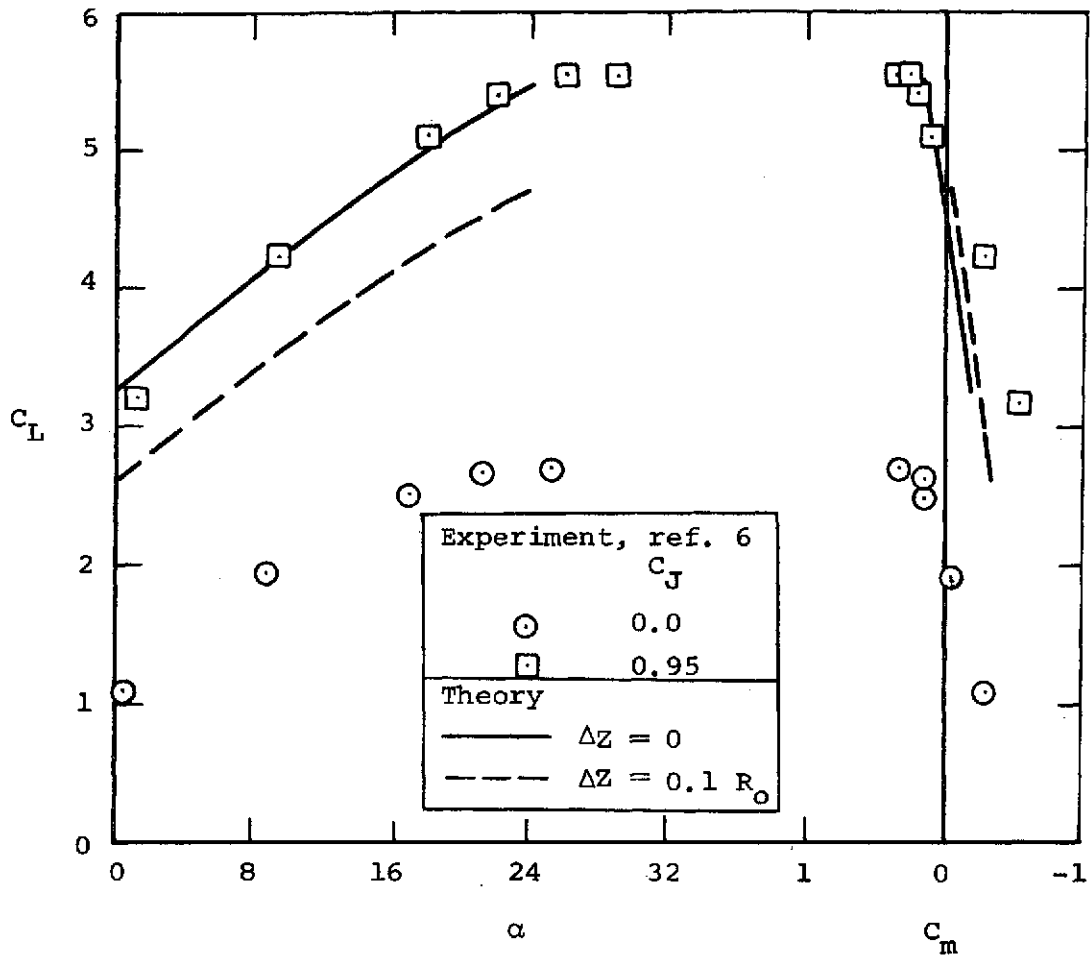
Figure 11.- Effect of height of jet model above wing surface
on the predicted lift and pitching-moment coefficients
on a two-engine USB model, tail off, $\delta_f = 55^\circ$.
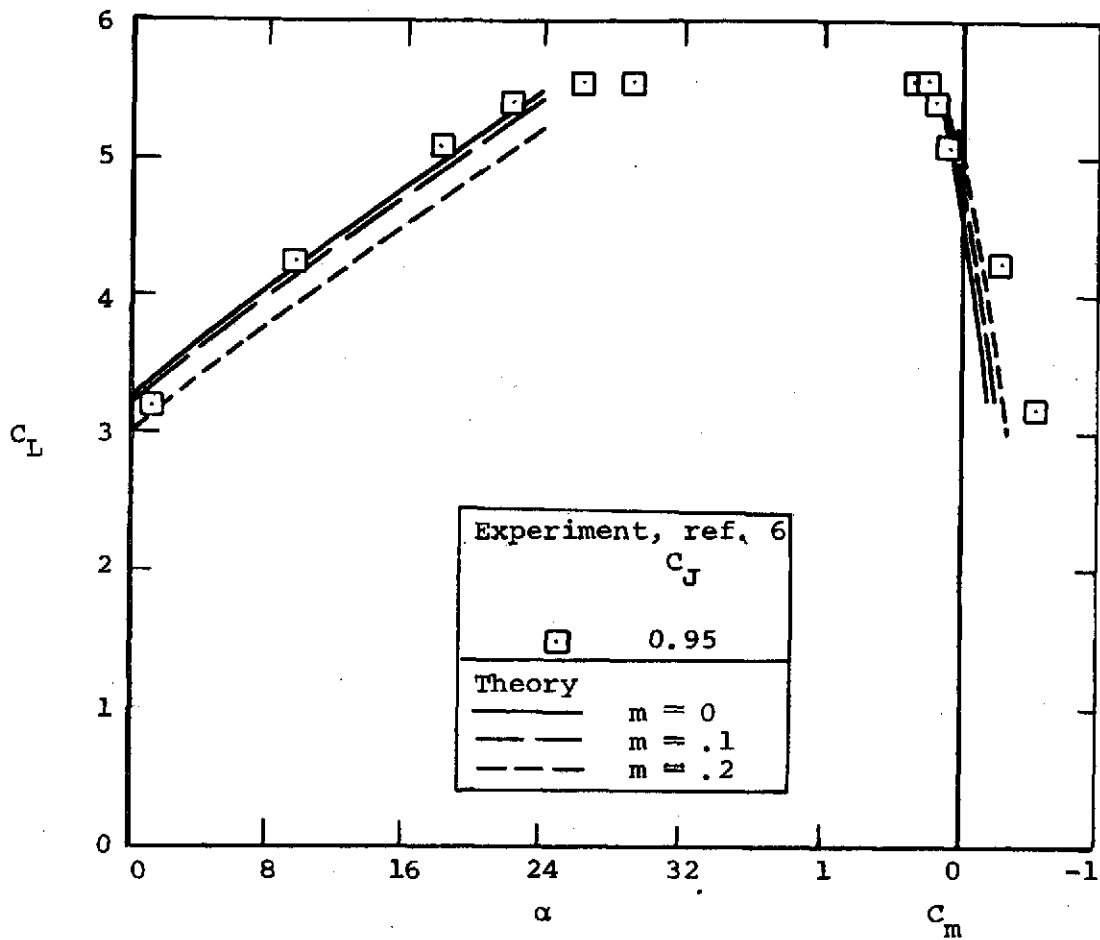
Figure 12.- Effect of jet spreading rate on the predicted lift and pitching-moment coefficients of a two-engine USB model, tail off, $\delta_f = 55^\circ$.

Separated model
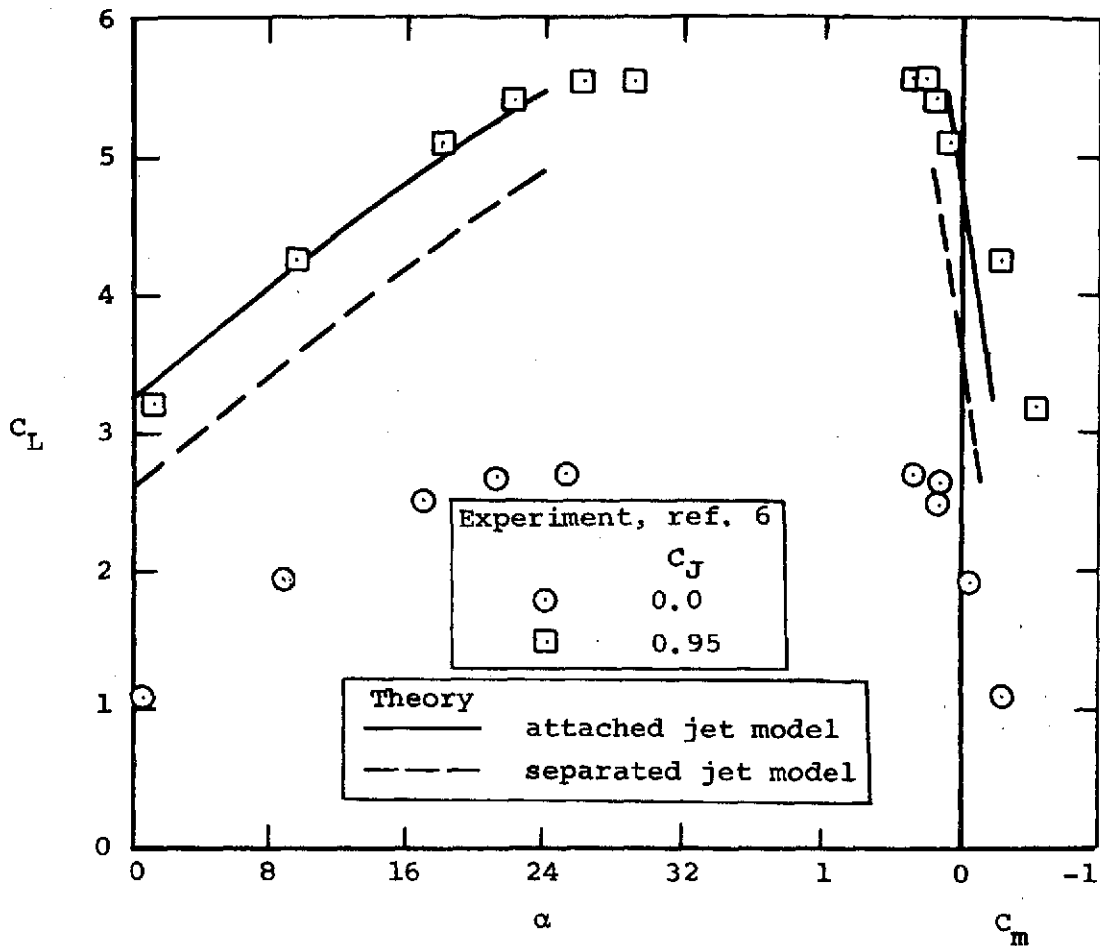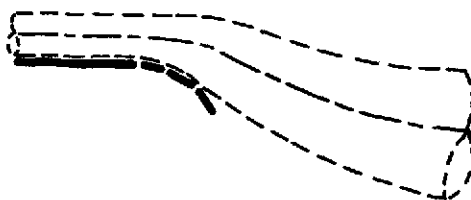
Figure 13.- Effect of jet separation on the predicted
lift and pitching-moment coefficients of a
two-engine USB model, tail off,
$\delta_f = 55^\circ$.
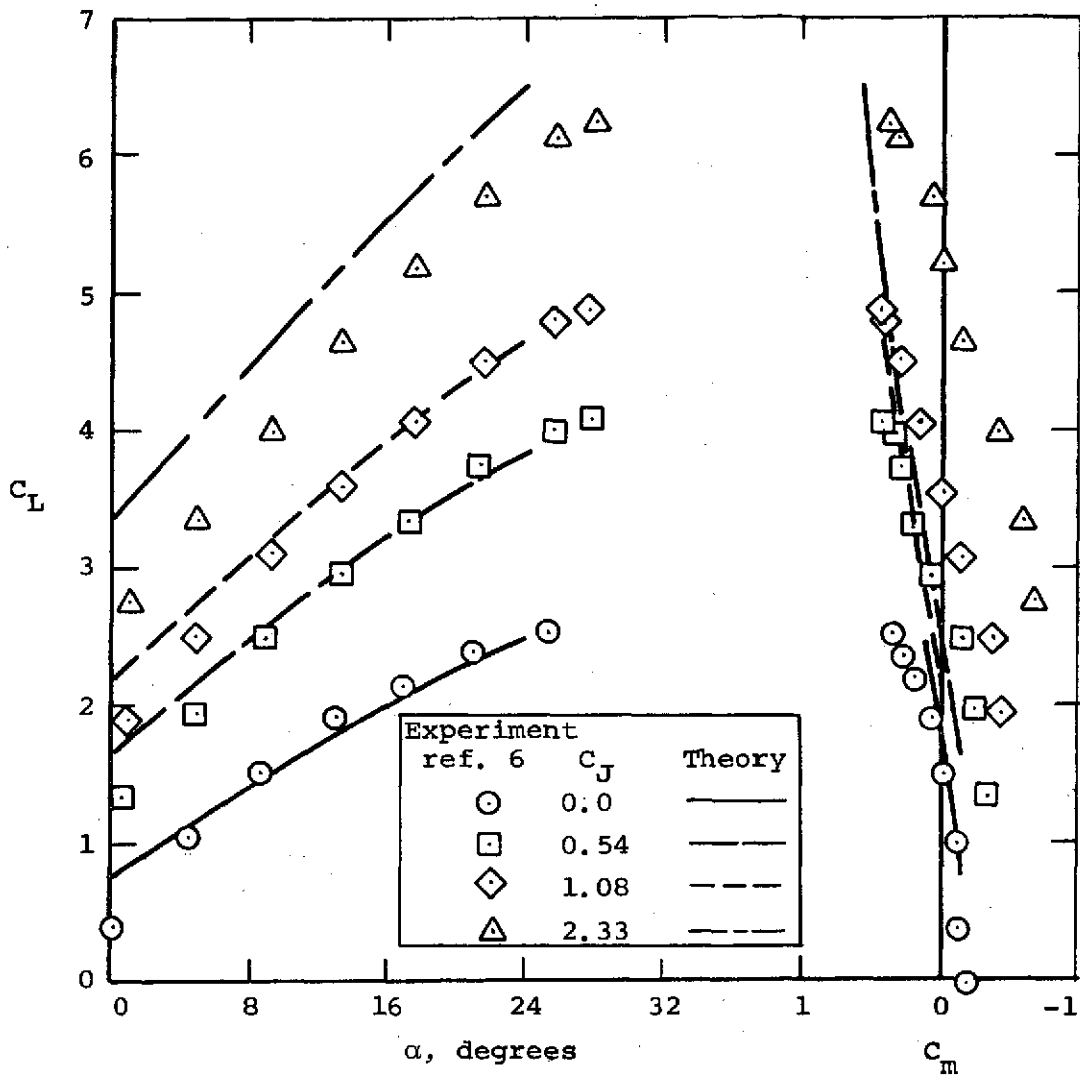
(a) Lift and pitching moment coefficients.

Figure 14.- Measured and predicted aerodynamic characteristics of
a two-engine USB model, tail off, $\delta_f = 30^o$.
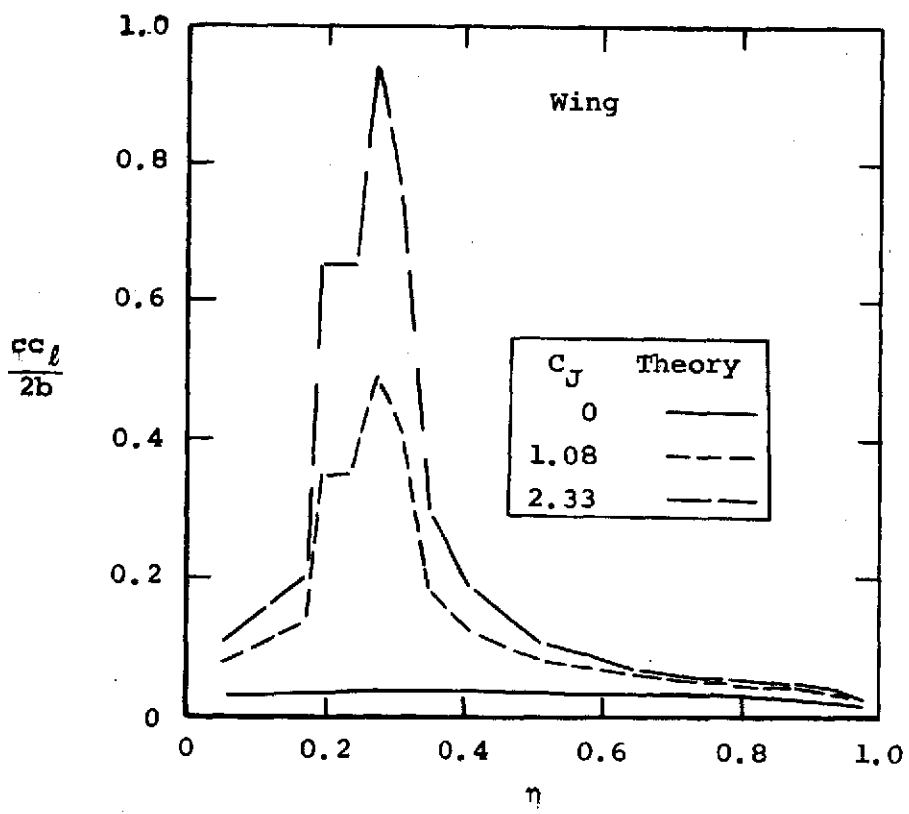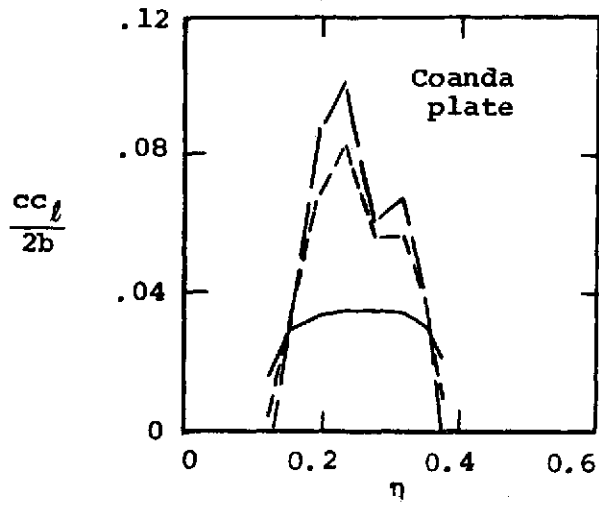
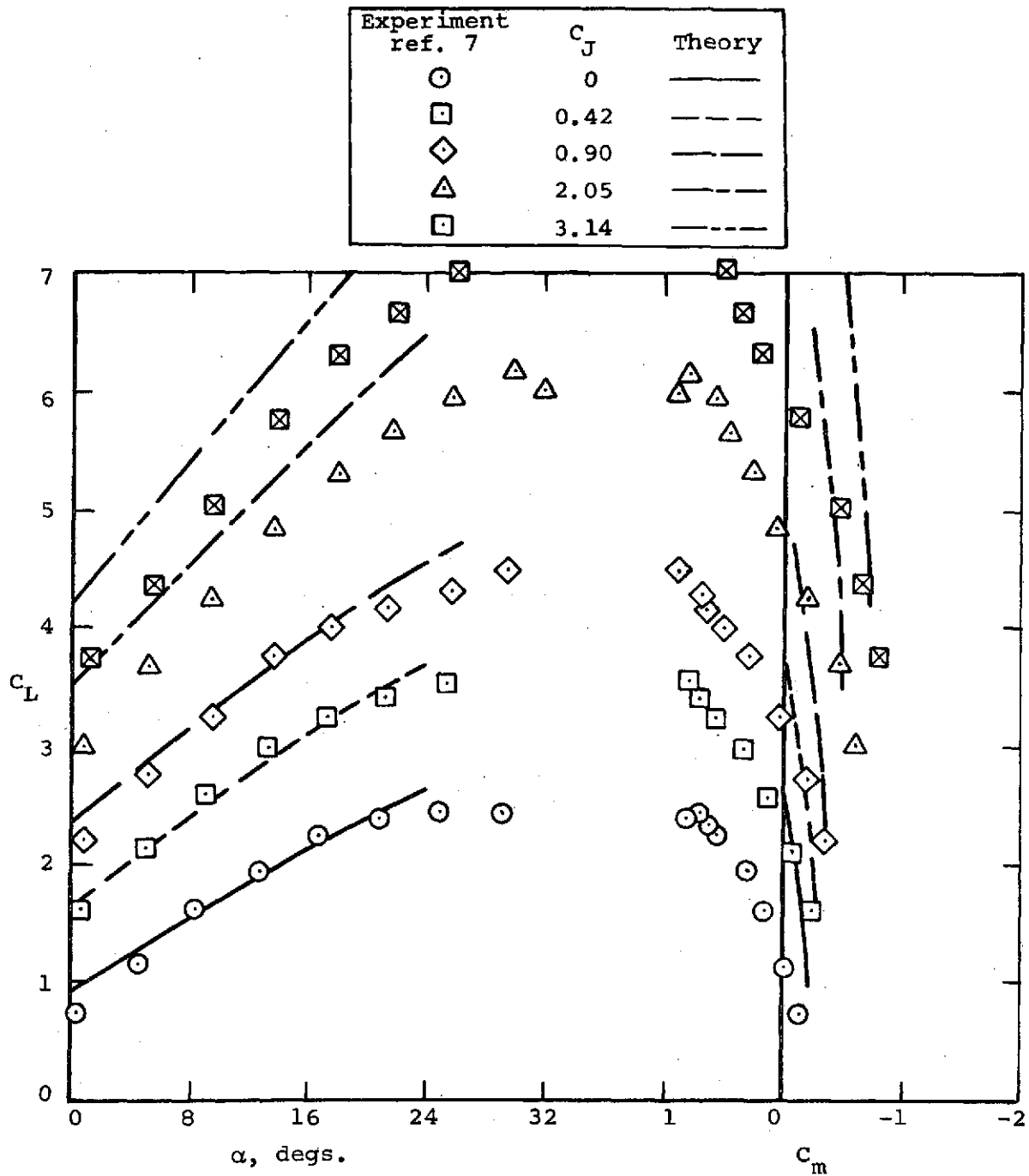(b) Span load distribution.
$\alpha = 0^\circ$

Figure 14.- Continued.

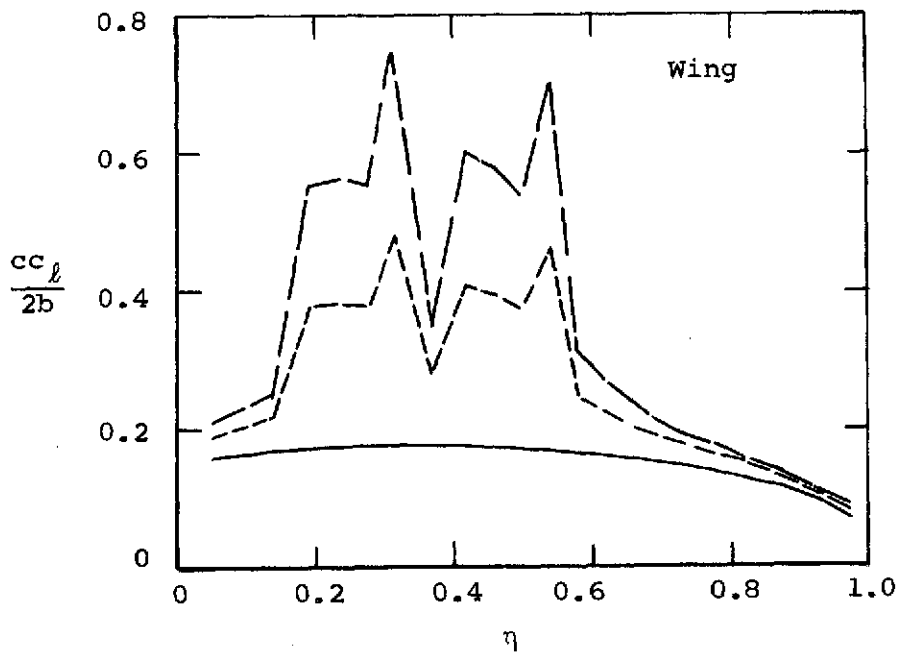Coanda plate

Wing

C_J	Theory
0	
1.08	
2.33	
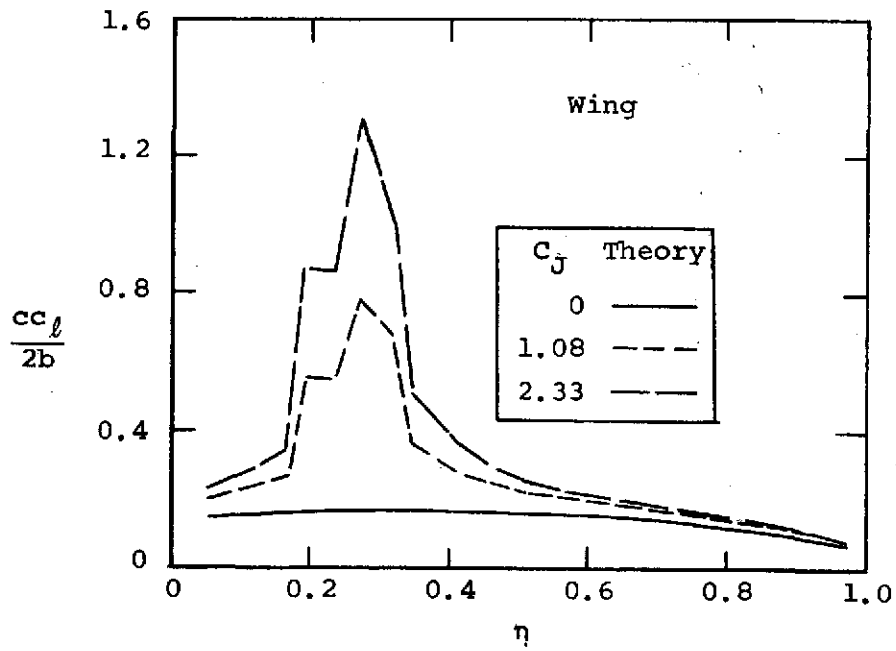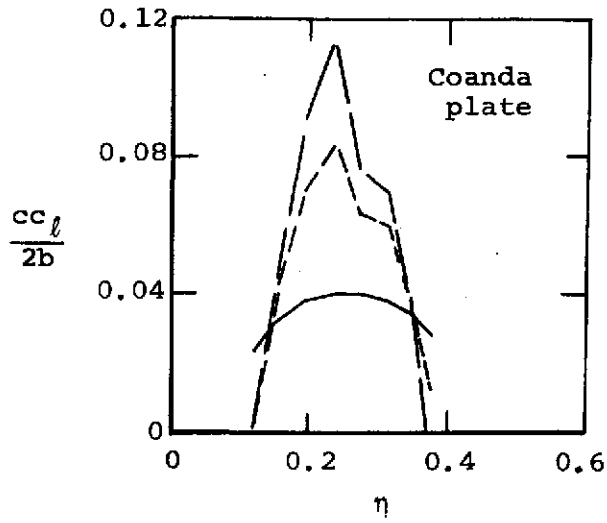
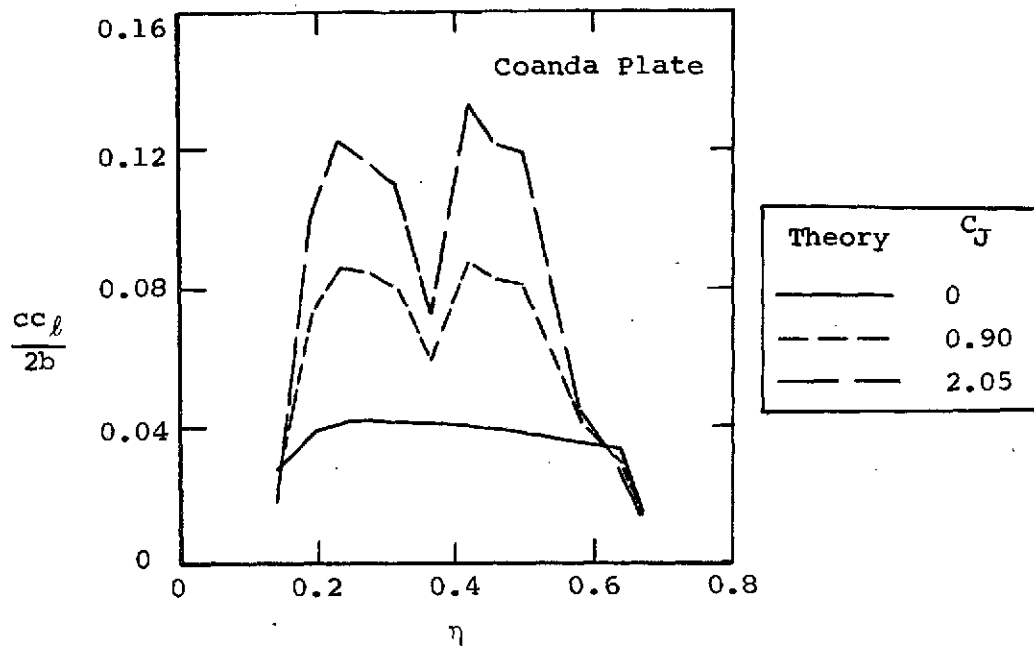(c) Span load distribution.
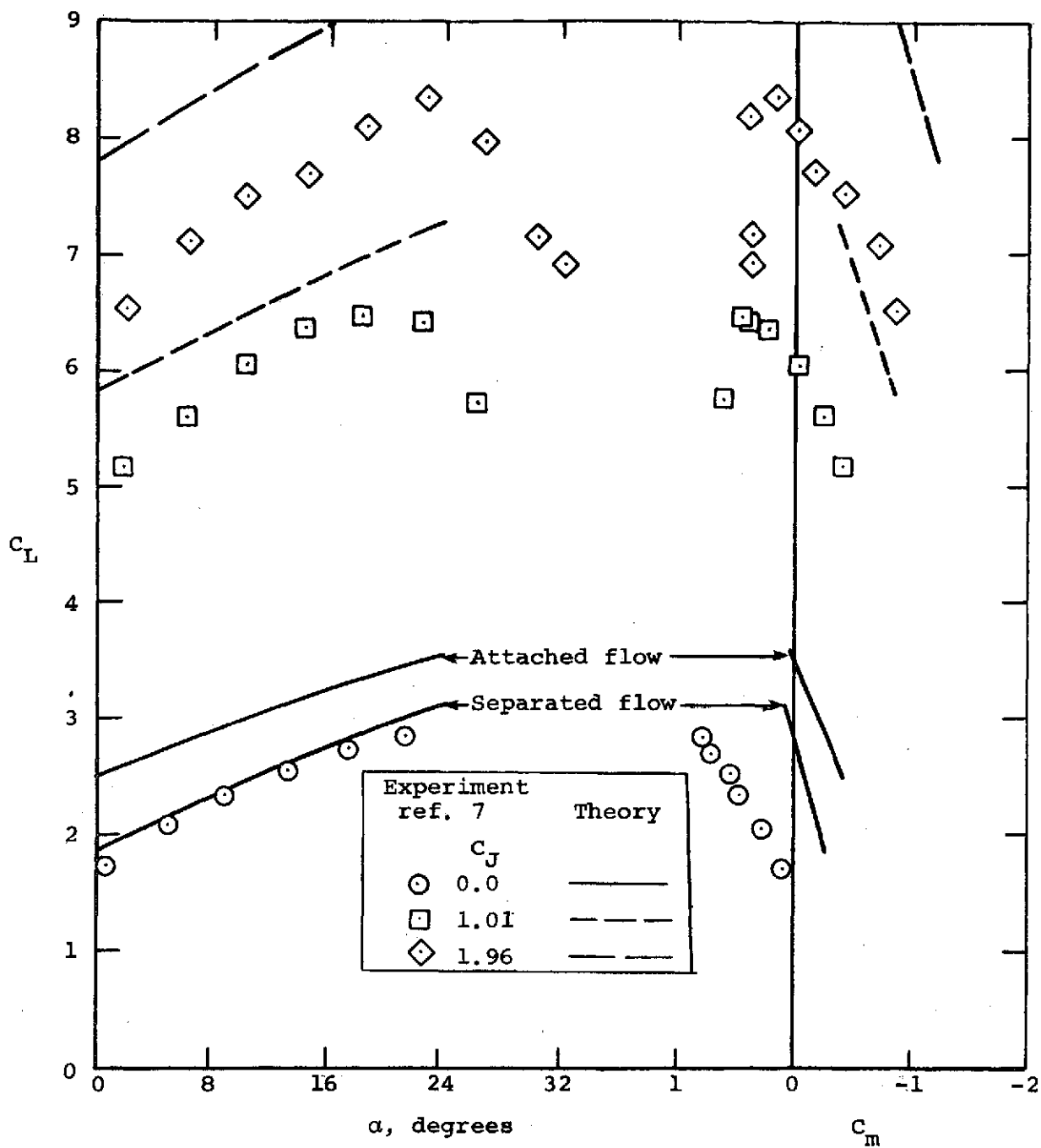$\alpha = 24^\circ$

Figure 14.- Concluded.
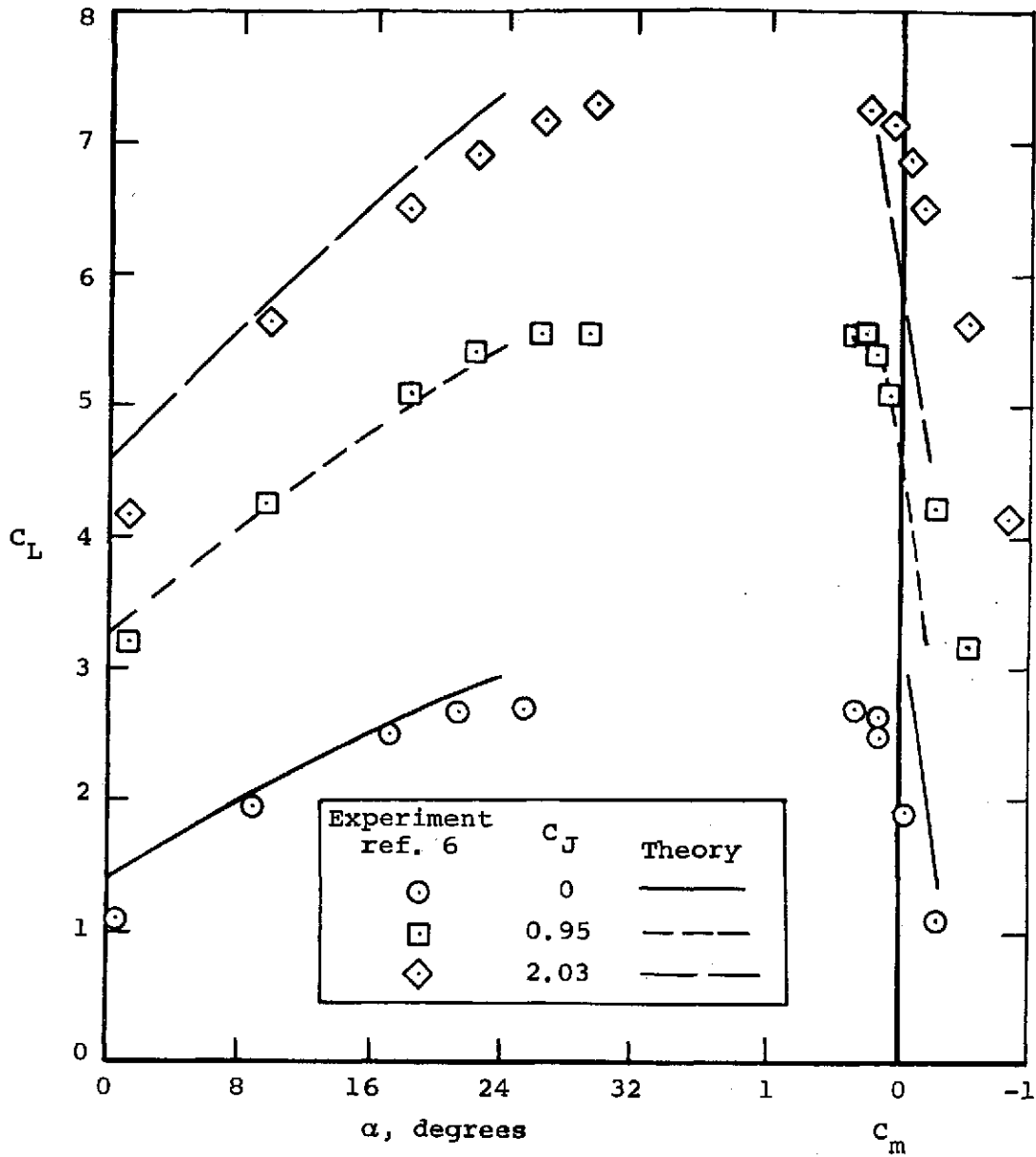
(a) Lift and pitching-moment coefficients.

Figure 15.- Measured and predicted aerodynamic characteristics
of a two-engine USB model, tail off,
$\delta_f = 55^o$.
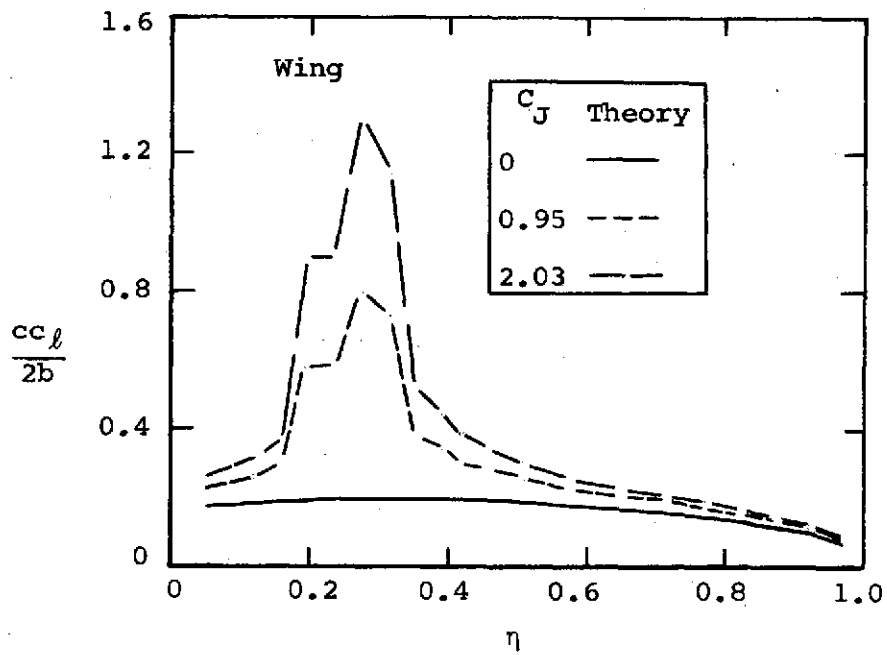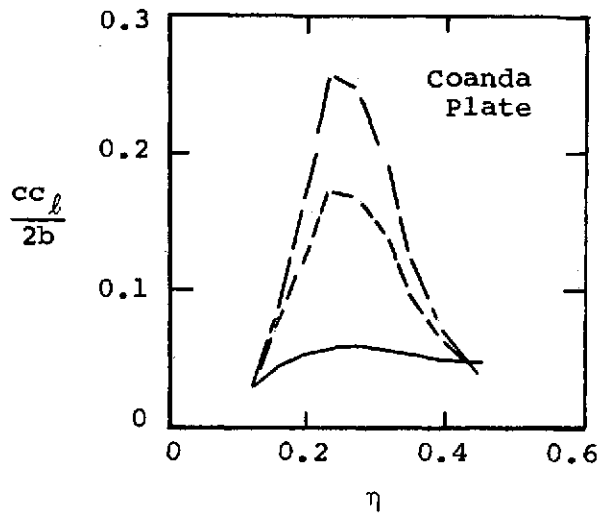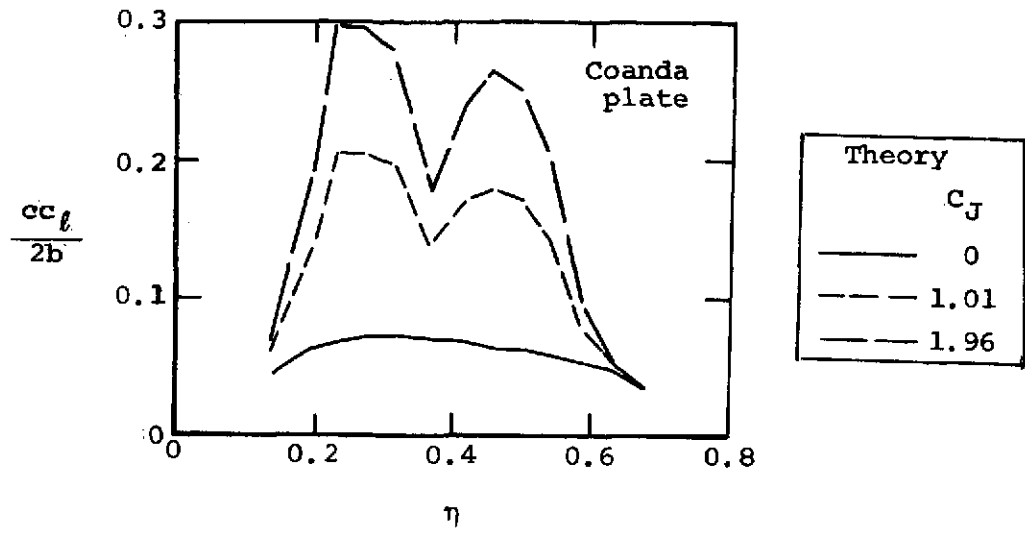
(b) Span-load distribution, $\alpha = 24^{o}$.

Figure 15.- Concluded.
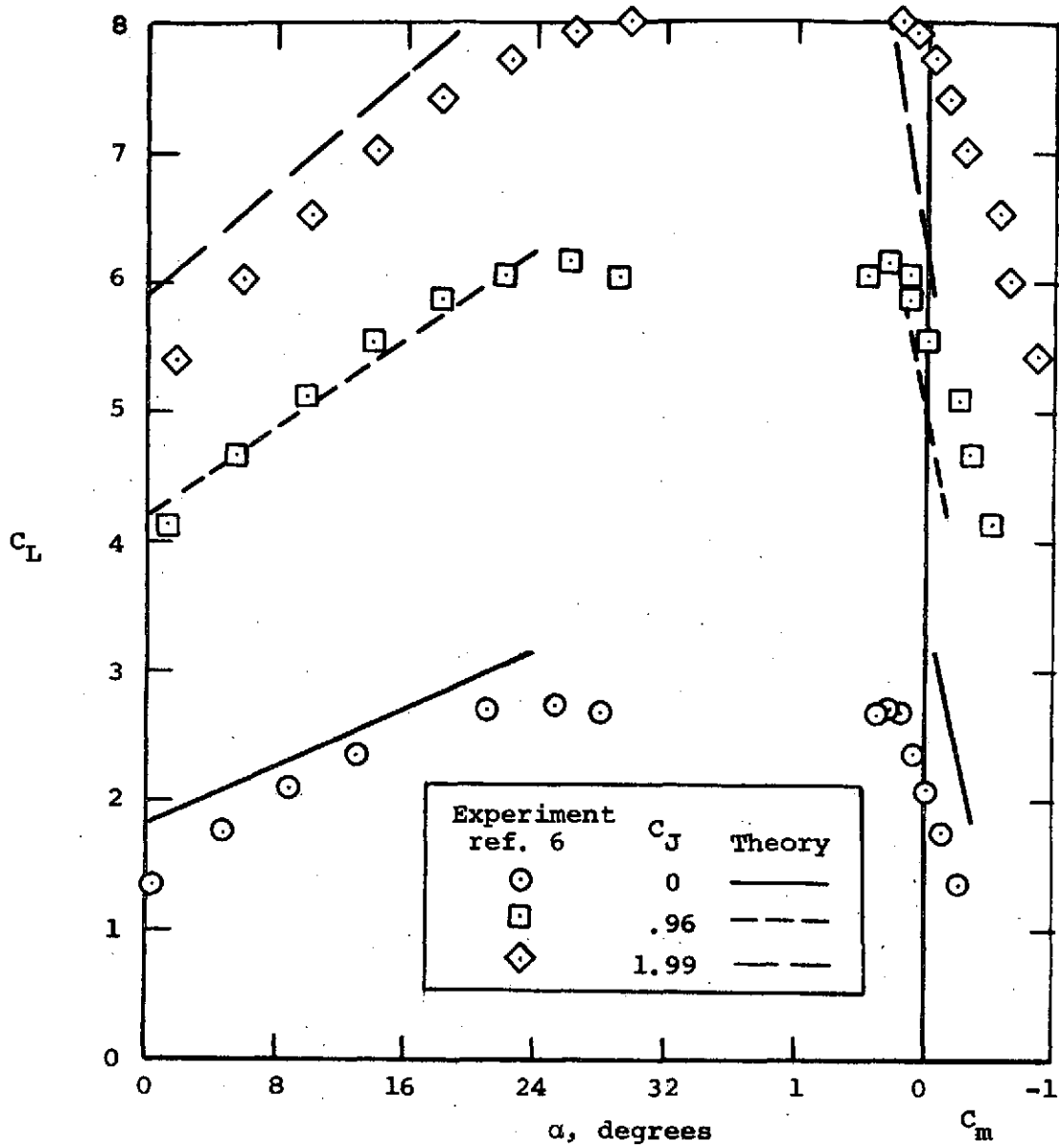
(a) Lift and pitching-moment coefficients.

Figure 16.- Measured and predicted aerodynamic characteristics of a two-engine USB model, tail off, $\delta_f = 75^o$.
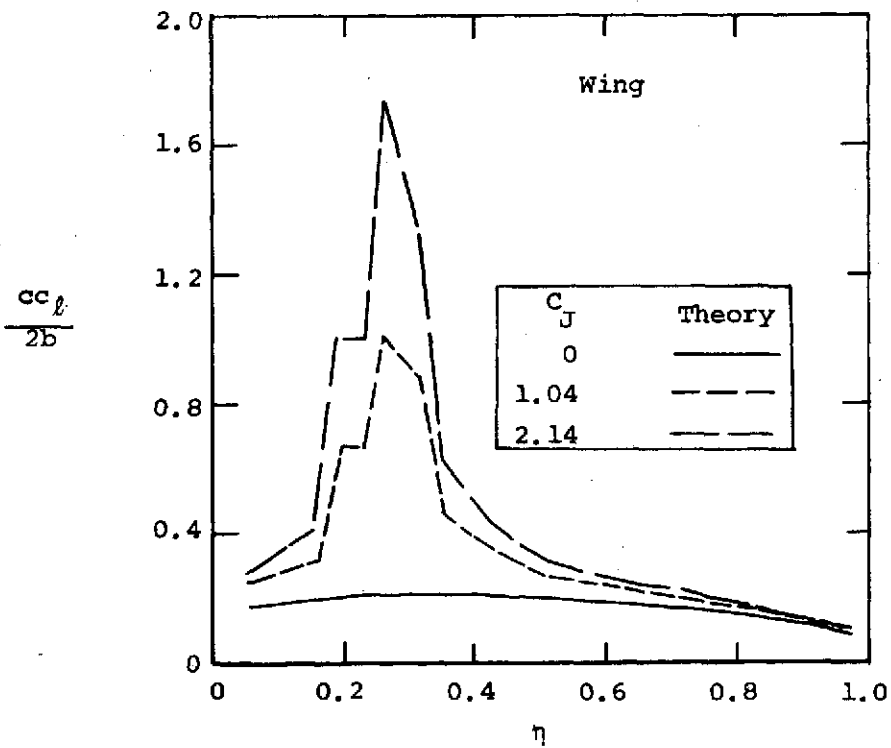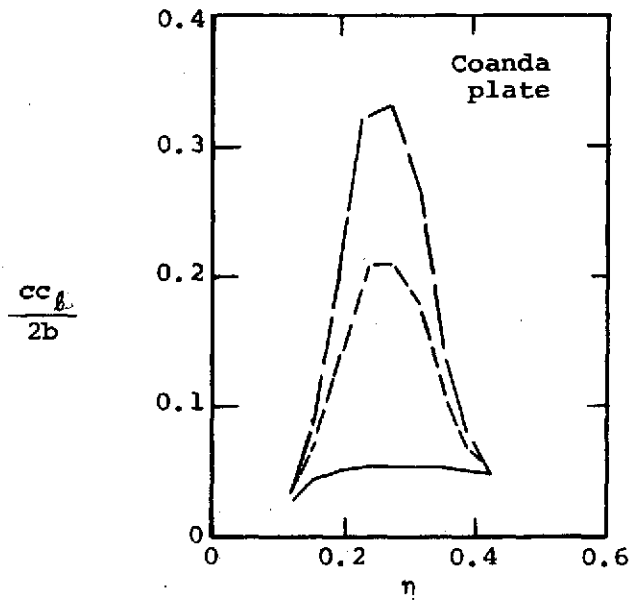
(b) Span load distribution, $\alpha = 24°$.

Figure 16.- Concluded.

Inboard nacelle

$\mathcal{C}_L$ $\mathcal{C}_L$ $\mathcal{C}_L$ $\mathcal{C}_L$

Outboard nacelle

All flaps are shown undeflected

$\mathcal{C}_L$ $\mathcal{C}_L$ $\mathcal{C}_L$ $\mathcal{C}_L$

Fuselage

Additional flap
extension for
$\delta_f = 90°$
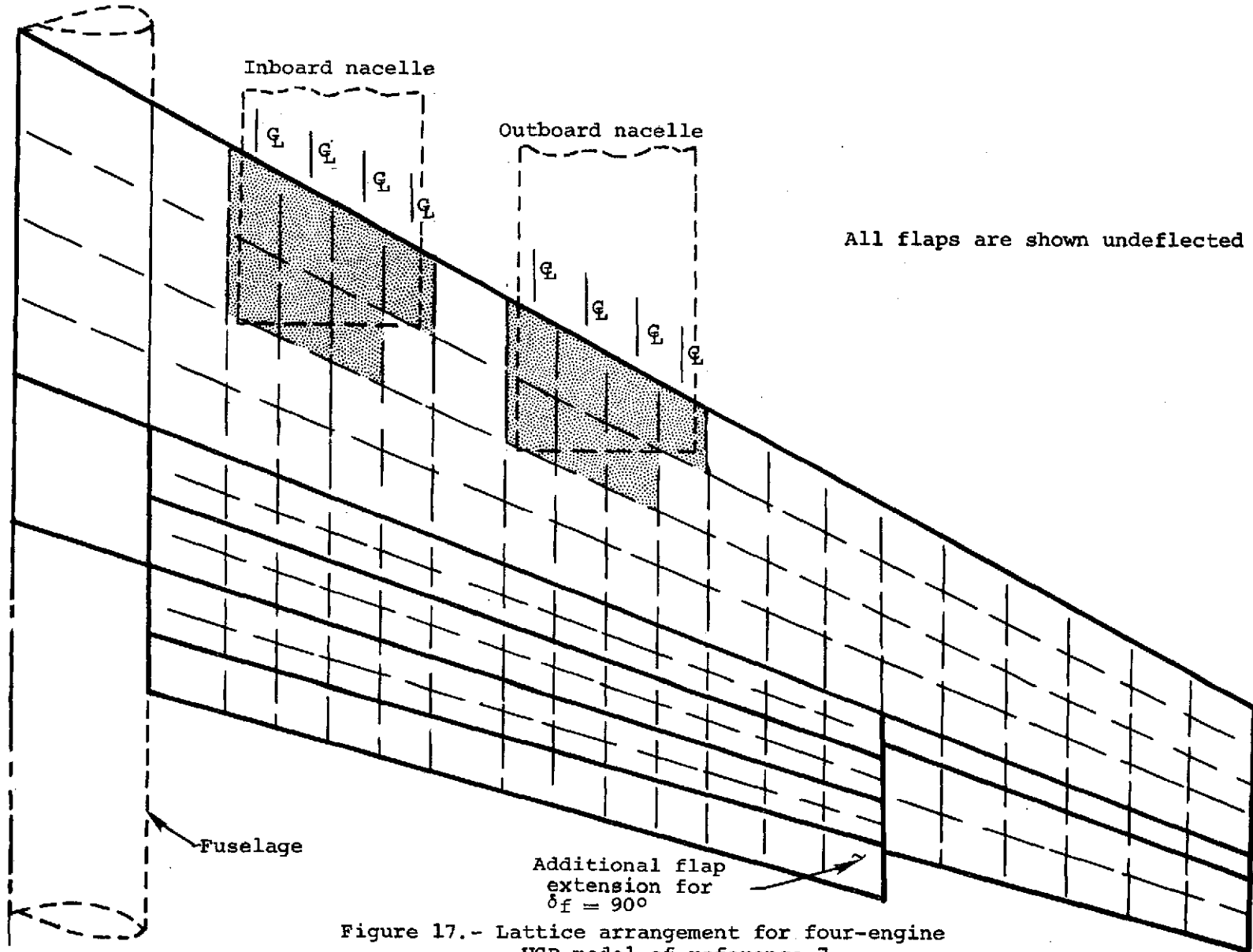
Figure 17.- Lattice arrangement for four-engine
USB model of reference 7.

(a) Lift and pitching-moment coefficients.

Figure 18.- Measured and predicted aerodynamic characteristics of a four-engine USB model, tail off, $\delta_f = 30^o$.

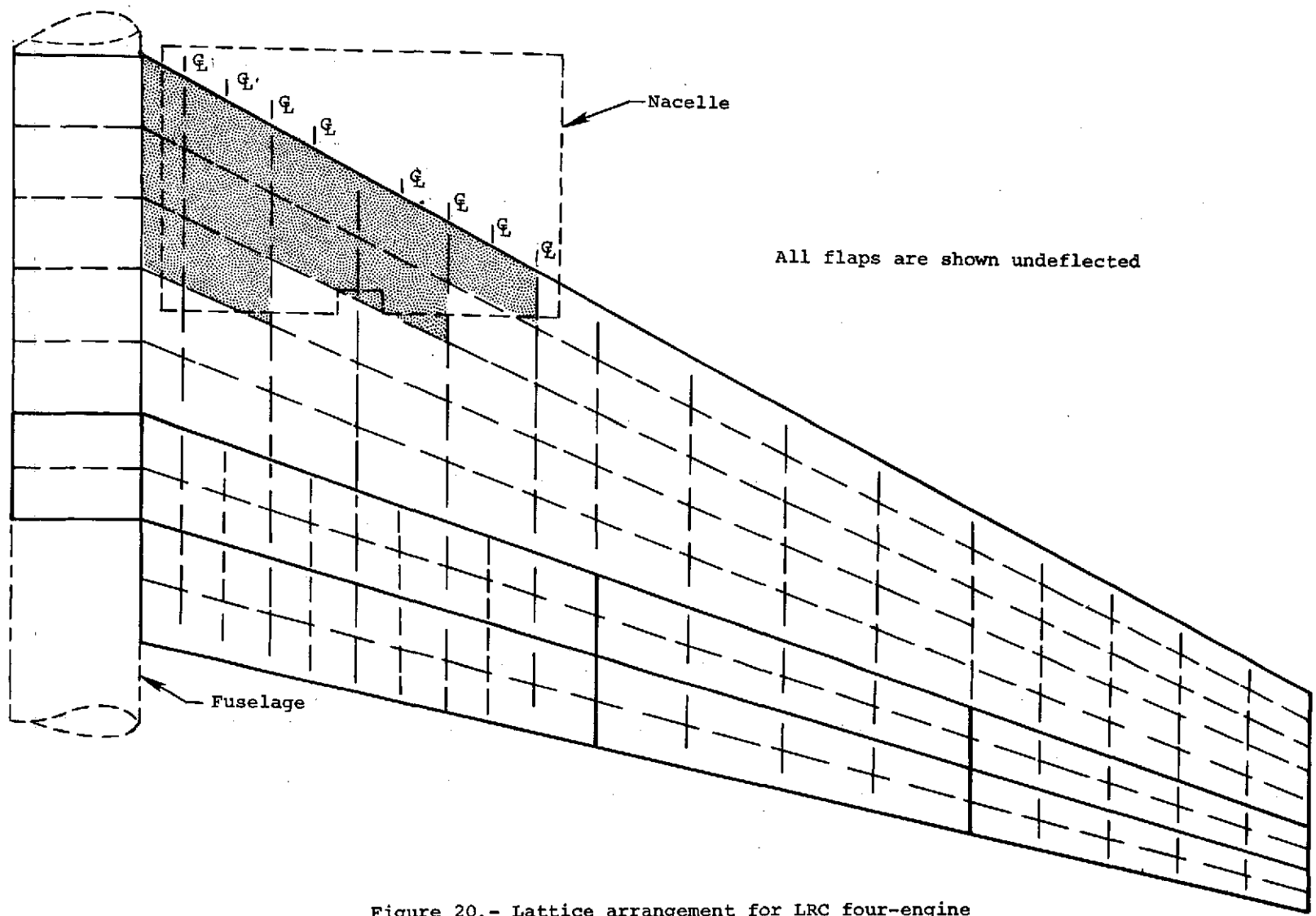(b) Span-load distribution, $\alpha = 24^{\circ}$.

Figure 18.- Concluded.

(a) Lift and pitching-moment coefficients.

Figure 19.- Measured and predicted aerodynamic characteristics of a four-engine USB model, tail off, $\delta_f = 90°$.
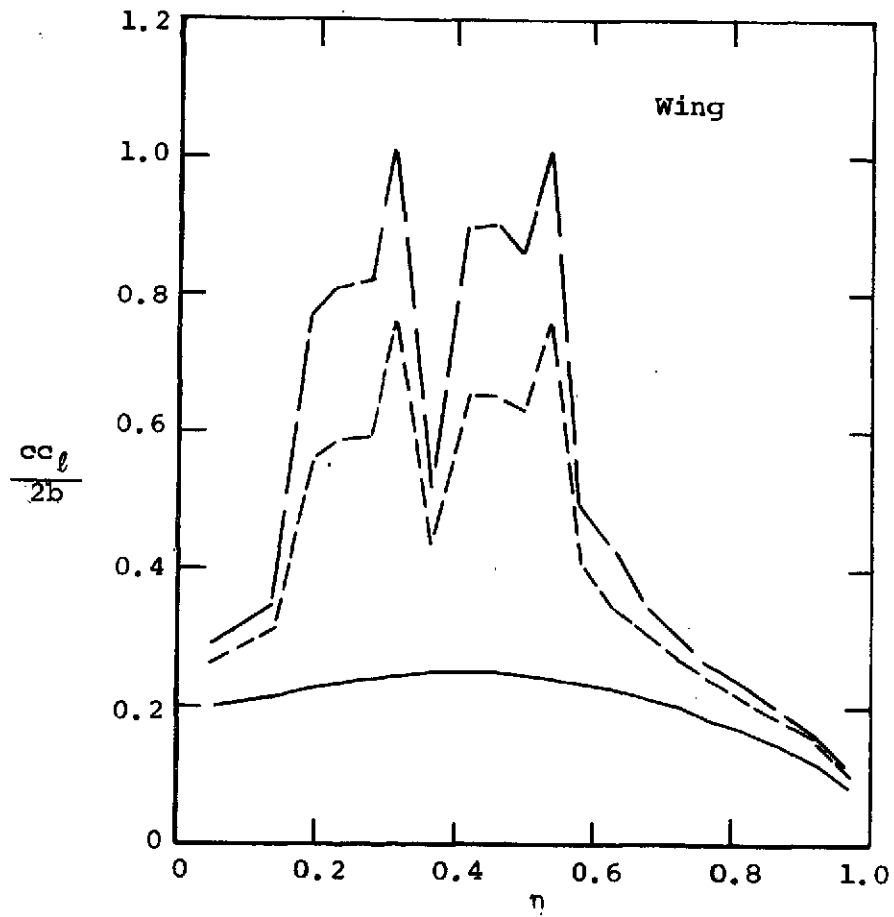
(b) Span load distribution, $\alpha = 24^\circ$.

Figure 19.- Concluded.

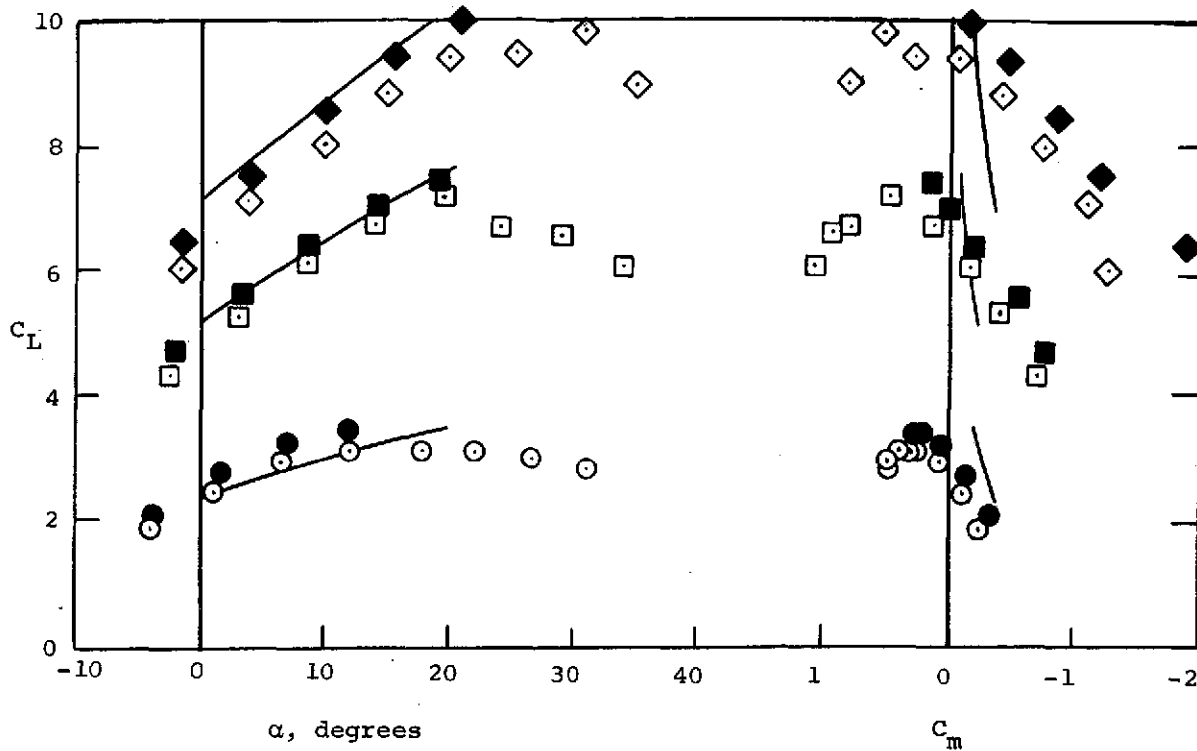Figure 20.- Lattice arrangement for LRC four-engine
USB model of reference 8.

Figure 21.— Measured and predicted lift and pitching-moment coefficients on a four-engine USB model, $\delta_f = 30°/30°/30°$.